A&A 589, A12 (2016)
DOI: 10.1051/0004-6361/201527236

Astronomy & Astrophysics

Seeking large-scale magnetic fields in a pure-disk dwarf galaxy NGC 2976

R. T. Drzazga[1], K. T. Chyży[1], G. H. Heald[2,3,⋆], D. Elstner[4], and J. S. Gallagher III[5]

[1] Obserwatorium Astronomiczne Uniwersytetu Jagiellońskiego, ul. Orla 171, 30-244 Kraków, Poland
e-mail: drzazga@oa.uj.edu.pl
[2] ASTRON, the Netherlands Institute for Radio Astronomy, Postbus 2, 7990 AA Dwingeloo, The Netherlands
[3] Kapteyn Astronomical Institute, University of Groningen, PO Box 800, 9700 AV Groningen, The Netherlands
[4] Leibniz Institute for Astrophysics Potsdam, An der Sternwarte 16, 14482 Potsdam, Germany
[5] Department of Astronomy, University of Wisconsin-Madison, 5534 Sterling, 475 North Charter St., Madison WI 53706, USA

Received 24 August 2015 / Accepted 11 February 2016

ABSTRACT

Aims. It is still unknown how magnetic field-generation mechanisms could operate in low-mass dwarf galaxies. Here, we present a detailed study of a nearby pure-disk dwarf galaxy NGC 2976. Unlike previously observed dwarf objects, this galaxy possesses a clearly defined disk. We also discuss whether NGC 2976 could serve as a potential source of the intergalactic magnetic field.
Methods. For the purpose of our studies, we performed deep multi-frequency polarimetric observations of NGC 2976 with the VLA and Effelsberg radio telescopes. Additionally, we supplement them with re-imaged data from the WSRT-SINGS survey for which a rotation measure (RM) synthesis was performed. A new weighting scheme for the RM synthesis algorithm, consisting of including information about the quality of data in individual frequency channels, was proposed and investigated. Application of this new weighting to the simulated data, as well as to the observed data, results in an improvement of the signal-to-noise ratio in the Faraday depth space.
Results. The magnetic field morphology discovered in NGC 2976 consists of a southern polarized ridge. This structure does not seem to be due to just a pure large-scale dynamo process (possibly cosmic-ray driven) at work in this object, as indicated by the RM data and dynamo number calculations. Instead, the field of NGC 2976 is modified by past gravitational interactions and possibly also by ram pressure inside the M 81 galaxy group environment. The estimates of total (7 μG) and ordered (3 μG) magnetic field strengths, as well as degree of field order (0.46), which is similar to those observed in spirals, suggest that tidally generated magnetized gas flows can further enhance dynamo action in the object. NGC 2976 is apparently a good candidate for the efficient magnetization of its neighbourhood. It is able to provide an ordered (perhaps also regular) magnetic field into the intergalactic space up to a distance of about 5 kpc.
Conclusions. Tidal interactions (and possibly also ram pressure) can lead to the formation of unusual magnetic field morphologies (like polarized ridges) in galaxies out of the star-forming disks, which do not follow any observed component of the interstellar medium (ISM), as observed in NGC 2976. These galaxies are able to provide ordered magnetic fields far out of their main disks.

Key words. galaxies: evolution – galaxies: magnetic fields – galaxies: dwarf – galaxies: individual: NGC 2976

1. Introduction

In low-mass dwarf galaxies, the conditions and efficiency of the magnetic field generation process are still not very well understood (see e.g. Chyży et al. 2011). In these objects, the influence of magnetic fields on the interstellar medium is expected to be even more important, because of their smaller gravitational potential and the possibility of gas escaping via galactic winds. On the other hand, dwarf galaxies rotate more weakly with more random motions, providing for a weak ω – effect. Therefore, there could be no large-scale dynamo at work in some dwarfs at all, as they are below the dynamo efficiency threshold (Gressel et al. 2008). In these objects, random magnetic fields could be produced by a small-scale dynamo action (Zeldovich et al. 1990).

The knowledge of properties of magnetic fields in dwarfs is also crucial for explaining the magnetization of the intergalactic medium (IGM). Kronberg et al. (1999) suggested in their "boiling universe" concept that low-mass galaxies were likely sources of primeval fields. However, Chyży et al. (2011) argued that for a sample of dwarf galaxies from the Local Group, these objects seem to be only able to magnetize their immediate neighbourhood. A similar conclusion was also drawn by Drzazga et al. (2011) in their studies of interacting galaxies as potential sources of the IGM's magnetic fields. Thus the question about the origin of the primeval magnetic fields and the role of dwarf galaxies in the magnetization of the Universe remains unanswered.

Only a handful of dwarf galaxies have been observed to date with respect to magnetic fields for which the dynamo concepts could be tested. As expected, in the very small and low-mass dwarfs IC 10 and NGC 6822 (linear size of 1 and 2 kpc, respectively) no large-scale (regular) magnetic fields have been detected to date (Chyży et al. 2003, 2011; Heesen et al. 2011), which indicates that these objects are below the efficiency threshold of the large-scale dynamo. In the more massive and larger dwarfs, NGC 4449 as well as in the Large Magellanic Cloud (LMC; of 7 and 10 kpc size, respectively), regular magnetic fields (of 8 and 1 μG, respectively) with fragments of some large-scale spiral structure, as evident signatures of large-scale

Current address: CSIRO Astronomy and Space Science, 26 Dick Perry Avenue, Kensington, Perth WA 6151, Australia.

$\alpha-\omega$ dynamo, were observed (Chyży et al. 2000; Gaensler et al. 2005). Some regular fields (of about 1 μG) were also found in the Small Magellanic Cloud (SMC; of 6 kpc size), but in this case, the field structure did not resemble any large-scale dynamo (Mao et al. 2008). However, as these three large dwarfs show distinct signs of strong tidal interactions, it is not clear whether and how gravitational interactions influenced the set-up of the large-scale dynamo process, and which conditions are appropriate for an efficient dynamo to occur in dwarfs.

To shed new light on the problem of the generation and evolution of magnetic fields in low-mass galaxies, multi-frequency, sensitive radio polarimetric observations of a dwarf galaxy NGC 2976 were performed. This is a dynamically simple, bulgeless, pure-disk object, with no discernible spiral arms (Simon et al. 2003) of SAc type (De Vaucouleurs et al. 1991) located at a distance of 3.6 Mpc. This galaxy seems to be a scaled version of the class of larger pure-disk spirals (e.g. Gallagher & Matthews 2002; Matthews & van Driel 2000). It has an absolute visual luminosity and disk size between those of SMC and LMC. The unique characteristics of NGC 2976 – its morphology of a typical spiral galaxy but its linear size and mass corresponding to those of dwarfs – makes it an ideal laboratory to study magnetic field-generation processes in low-mass galaxies. The total power (TP) radio emission of NGC 2976 was observed at 1.4 GHz with the Very Large Array (VLA) by Condon (1987). This galaxy was also included in the WSRT-SINGS polarimetric survey (Heald et al. 2009; Braun et al. 2010), within which deep and high-resolution observations were performed using the WSRT. However, the relatively small mass and the dwarf-like, rather than spiral character of NGC 2976, went unnoticed in previous studies.

NGC 2976 is a member of the M 81 galaxy group, located close to its centre. However, unlike the Magellanic Clouds and NGC 4449, NGC 2976 has probably not been greatly disturbed for a long time, as it shows very regular U, B, and V isophotes in the outer disk (Bronkalla et al. 1992), its H I velocity field is undistorted, and its velocity dispersion is small (11 km s^{-1}, Stil & Israel 2002b). Hence, the conditions for the magnetic field generation process (e.g. galactic dynamics, size, mass, star formation rate (SFR), etc.) can be constrained for this object without the strong influence of gravitational or ram pressure interactions. Such well-established dynamo conditions are of primary significance in building up theoretical concepts of the dynamo theory (Brandenburg & Subramanian 2005) as well as in explaining the magnetic structures that have been observed in dwarfs.

Studies of magnetic fields in dwarf galaxies are observationally difficult, as these objects are usually radio-weak (e.g. Chyży et al. 2011). Hence, we used sensitive instruments: the VLA[1] (USA) and 100-m Effelsberg radio telescope[2] (Germany) to observe NGC 2976. Additionally, we supplemented our observations with the spectro-polarimetric data from the WSRT-SINGS survey (Heald et al. 2009). The detailed account of these observations and the data reduction are given in Sect. 2. In Sect. 3 the results are presented. Discussion and conclusions of the results are shown in Sects. 4 and 5, respectively.

[1] The National Radio Astronomy Observatory is a facility of the National Science Foundation operated under cooperative agreement by Associated Universities, Inc.

[2] The 100-m telescope at Effelsberg is operated by the Max-Planck-Institut für Radioastronomie (MPIfR) on behalf of the Max-Planck-Gesellschaft.

2. Observations and data reduction

2.1. VLA

NGC 2976 was observed with the VLA in L band in C, DnC, and D configurations (Table 2). The total on-source time, as calculated from the schedule and dynamic times, was about 16 hours. The observations were performed in full polarization mode using two 50 MHz width "intermediate frequency" channels centred at 1385.100 and 1464.900 MHz. The data were reduced with the AIPS package[3], following the standard procedure. The flux scale and position angle of polarization were calibrated using the amplitude calibrator (0521+166;3C 138/1331+305;3C 286). The phase calibrator (0841+708) was used to find gain, phase, and polarization leakage solutions. Each of the datasets specified in Table 2 was calibrated in this way separately, and then self-calibrated in phase-only. After checking for consistency between the datasets, they were concatenated and self-calibrated in phase, as well as in amplitude and phase.

In the final stage, imaging with the AIPS task IMAGR was performed for all the Stokes parameters using Briggs' robust weighting of 1 and −5. The obtained Q and U maps were combined within the task COMB to form maps of polarized intensity that were corrected for positive bias (PI = $\sqrt{Q^2+U^2}$) and polarization angle (PA = 0.5 arctan(U/Q)). The rms sensitivity (for imaging with robust 1) is 20 μJy/beam for the total power intensity, and 9 μJy/beam for the polarized intensity (PI).

2.2. Effelsberg

NGC 2976 was observed with the 100-m Effelsberg radio telescope at 4.85 and 8.35 GHz. At 4.85 GHz, a two-horn secondary focus system with bandwidth of 0.5 GHz was used, recording data in four channels/horn. Two of these channels recorded the total power signal, while the others recorded signals in Stokes Q and U. For the object, 24 coverages (maps) in Az/Alt frame were obtained. However, only 12 of them were suitable for polarization studies (Table 3). At 8.35 GHz, a 1.1 GHz bandwidth single-horn receiver was used, also recording data in four channels (see above). In this case, 66 coverages in the right ascension-declination (RA/Dec) frame were obtained. Unfortunately, nearly half of the data (Table 3) were unusable, owing to strong radio frequency interference-like (RFI) spikes near the target. At both the observation frequencies, corrections of telescope pointing were made about every 1.5 h by scanning a nearby strong point radio source.

We performed data reduction in the standard way by applying the NOD2 package (Haslam 1974). First, all coverages at both the frequencies were edited to remove any RFI and align baselines to the common level; then the data at 4.85 GHz from both horns were averaged using the software beam-switching technique (Morsi & Reich 1986) and transformed to the RA/Dec frame (for 8.35 GHz data this step was not necessary, see above). In the next stage of data reduction, all usable coverages (Table 3) were combined using the spatial frequency weighting method (Emerson & Gräve 1988). In the final stage, all Stokes parameter maps at both wavelengths were digitally filtered to remove Fourier spatial frequencies, which correspond to noisy structures that are less than the beam sizes and then transformed to the FITS format. Further processing that included flux scale calibration and the formation of polarized intensity (corrected for positive bias) and polarization angle maps was performed in the

[3] http://www.aips.nrao.edu/index.shtml

Table 1. Basic properties of NGC 2976.

Name	*Hubble*[1] type	Inclination[1] [deg.]	Linear size[2] [kpc]	H I mass[3] [10^8 $M_\odot$]	*SFR*[3] [$M_\odot$/yr]
NGC 2976	SAc	65	6	1.8 (1.5[(4)])	0.2

Notes. [(1)] Heald et al. (2009); [(2)] estimates based on distances taken from Kennicutt et al. (2003) and angular sizes (D_{25}) from Heald et al. (2009); [(3)] Kennicutt et al. (2003); [(4)] Stil & Israel (2002b).

Table 2. Parameters of the VLA observations of NGC 2976 at 1.43 GHz.

Type of obs.	Obs. date	Configuration	Integr. time [h]	Amp. cal.	Phas. cal.
Schedule	28 Aug. 2009	C	5.8	0521+166/1331+305	0841+708
Dynamic	18 Sep. 2009	DnC	0.7	0521+166	0841+708
Dynamic	20 Sep. 2009	DnC	1.4	0521+166	0841+708
Dynamic	21 Sep. 2009	DnC	1.6	0521+166	0841+708
Dynamic	01 Oct. 2009	DnC	1.6	0521+166	0841+708
Schedule	31 Oct. 2009	D	1.5	1331+305	0841+708
Dynamic	06 Nov. 2009	D	1.6	1331+305	0841+708
Dynamic	11 Nov. 2009	D	1.6	0521+166	0841+708

Table 3. Parameters of the Effelsberg observations of NGC 2976 at 4.85 and 8.35 GHz.

Obs. freq. GHz	Obs. date	Map size arcmin	Total/good(TP)/good(PI) coverages	$S_{\rm TP}$ mJy	$S_{\rm PI}$ mJy	rms (TP) mJy/beam	rms (PI) mJy/beam
4.85	May 2009 May 2010 May 2011	35 × 25	24/21/12	30.0 ± 1.4	1.6 ± 0.4	0.45	0.08
8.35	May 2011	21 × 21	66/35/35	19.3 ± 0.9	n.a.	0.23	0.08

AIPS package. At both frequencies, the flux scales were calibrated using 3C 286, based on the assumption that its flux is 7.47 Jy at 4.85 GHz and 5.27 Jy at 8.35 GHz (as provided in the VLA Calibrator List[4]). The obtained rms noise levels are given in Table 3.

2.3. Re-analysis of the WSRT-SINGS data

We also made use of the calibrated WSRT-SINGS polarimetric uv data in the 18 cm and 22 cm bands (for details see Heald et al. 2009). The data were re-imaged by applying the Miriad software using the Briggs robust weighting of 1.0. The Q and U frequency data cubes containing 702 frequency channels obtained in this way were convolved to the resolution of 48.6 × 45.0 , providing a high sensitivity to extended radio structures. Then, for the Q and U data cubes, rotation measure synthesis (RM synthesis; Brentjens & de Bruyn 2005) was performed applying a new weighting scheme that takes the quality of individual frequency channels into account (see Appendix A for details).

The resolution in Faraday depth that was obtained for the frequency coverage of the WSRT-SINGS survey is about 144 rad m^{-2}, whereas the sensitivity to extended structures in Faraday space (at which 50% of polarized flux can be recovered) is about 110 rad m^{-2}. The maximum Faraday depth that could be sampled in the Faraday domain is about 1.7×10^5 rad m^{-2}. We did not expect polarized emission at such high depths so, the Faraday domain was sampled within a range of −500 to +500 rad m^{-2} every 2.5 rad m^{-2}. As the rotation measure transfer function (RMTF) shows a high level of side-lobes (of about 80%, see Sect. A.4) owing to the gap in frequency coverage between 18 cm and 22 cm data bands, the RM-CLEAN deconvolution method (Heald et al. 2009) was used. With this algorithm, the $Q(\phi)$ and $U(\phi)$ cubes were cleaned down to the 1-sigma noise level and then restored with a Gaussian beam of the same width as the main RMTF lobe. After cleaning Q and U data cubes, we calculated the polarized intensity map for the studied object (not corrected for the positive bias as negligible in this case). This map was obtained as a maximum of PI signal over all sampled Faraday depths for each line of sight. We also computed B-vectors, maximum Faraday depth (for the maximum of PI signal), and magnetic field vector distribution maps. The B-vectors map was calculated for the effective frequency of about 1.5 GHz to which all polarization vectors were de-rotated. This approach is applied because, for the given resolution in Faraday domain and signal-to-noise ratio of at least 4, the maximum Faraday depth error is large, about 18 rad m^{-2}, which prevents us from directly obtaining reliable information about intrinsic directions of magnetic field vectors (see Brentjens & de Bruyn 2005).

3. Results

3.1. 1.43 GHz

Our sensitive polarimetric VLA observation of NGC 2976 results in a detection of some very extended radio emission surrounding the object (Fig. 1). This radio extent of the galaxy was not known earlier, as previously only a total power emission closely related to its optical disk was obtained (Condon 1987; Niklas 1995; Stil & Israel 2002a; Heald et al. 2009). In the low-resolution total power map (Fig. 1), the brightest emission coincides with the sharpened disk (i.e. a disk possessing sharp truncation edge; Williams et al. 2010) of the NGC 2976, and the maximum is well correlated with two bright H II regions

[4] https://science.nrao.edu/facilities/vla/observing/callist

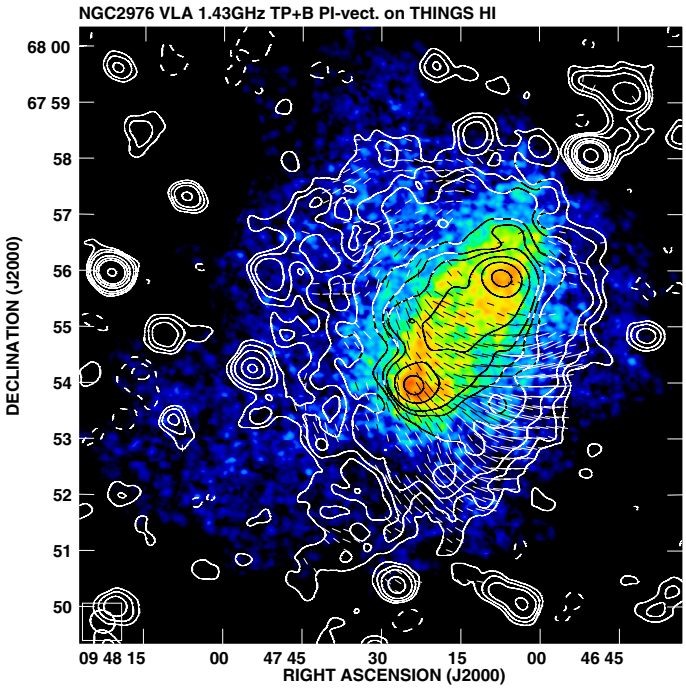

Fig. 1. Total-power contours and apparent B-vectors (not corrected for Faraday rotation) of polarized intensity of NGC 2976 (obtained with Robust = 1 weighting) at 1.43 GHz superimposed on the H I map (from the THINGS survey, Walter et al. 2008) shown in a logarithmic scale. The H I map resolution is 7.41″ × 6.42″ HPBW, position angle of the beam is 71.8 degrees. The contours levels are (−5, −3, 3, 5, 8, 16, 24, 32, 64, 128, 256) × 20 (rms noise level) μJy/beam. A vector of 10″ length corresponds to the polarized intensity of about 42 μJy/beam. The map resolution is 26.8″ × 23.5″ HPBW, while the beam position angle is 62 degrees.

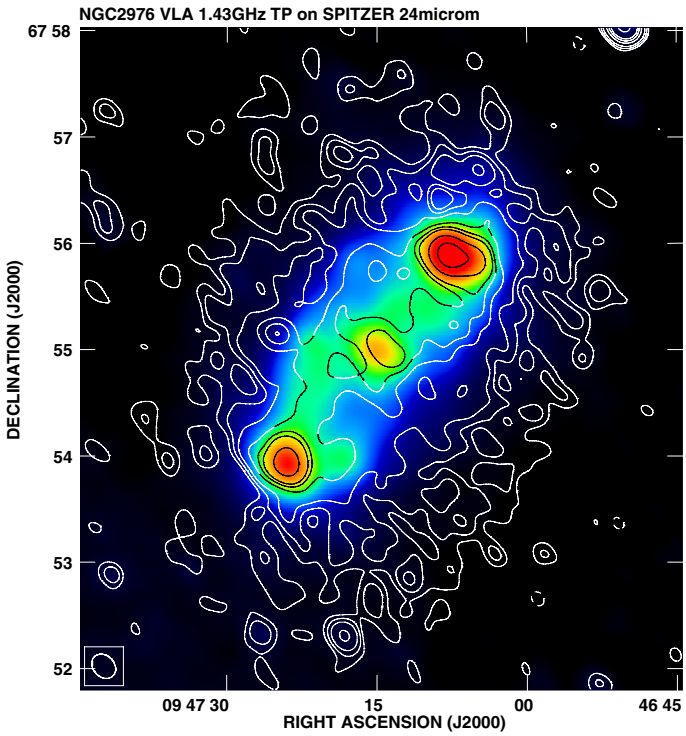

Fig. 2. Total-power contours of NGC 2976 (obtained with Robust = −5 weighting) at 1.43 GHz superimposed on the *Spitzer* 24 μm image (Kennicutt et al. 2003), shown in logarithmic scale and convolved to the resolution of radio data. The contours levels are (−5, −3, 3, 5, 8, 16, 24, 32, 64, 128) × 20 (rms noise level) μJy/beam. The map resolution is 15.1″ × 11.9″ HPBW, while the beam position angle is 42 degrees.

located at the edges of the object. This is even more visible in the high-resolution (of about 0.26 kpc) map (Fig. 2) superimposed on the 24 μm infrared image from *Spitzer* (Kennicutt et al. 2003). There is a good correspondence between the images in both wavelengths.

Beside the stellar disk, the total power radio emission (in the lower resolution map, Fig. 1) extends in the north-eastern direction, where a low-brightness signal of about 60 μJy/beam (3 × rms noise level) resides. Radio emission at a similar level is also observed in the southern part of the galaxy. However, here its extension is smaller and brighter than in the opposite direction. The total power radiation of NGC 2976 corresponds well to its H I distribution (Fig. 1) in the NE and SW directions. However, radio emission does not follow the outer SE extension and the spur of H I in the north (see also Chynoweth et al. 2008).

The distribution of polarized intensity in NGC 2976 (Fig. 3) is even more surprising than the total power one. Most of the observed polarized emission (more than 60%) comes from the south-western part of the object, where the polarization degree reaches 50%. We note that this number does not take into account the regions within the object close to the total power intensity at the level of 3 × rms, where the polarization degree has unphysical values as high as 100%. This is due to the higher sensitivity of the polarized intensity map, which is not bounded by the confusion limit. The brightest southern PI region was also detected by Heald et al. (2009) in their high-resolution WSRT-SINGS survey (see also Sect. 3.5). The polarized signal is weaker in the disk, and appears only in its southern part. In the northern part of NGC 2976, the distribution of polarized signal forms a curved arc structure. A convolution of the Q and U Stokes parameters maps to the lower resolution of 45″ and then computing the PI map that resulted from them (Fig. 4) enabled us to also detect a polarized extension in the southern part of the object. Southern and south-eastern extensions coincids with the H I tail and the northern tip of PI corresponds to the northern H I spur, which is visible in Fig. 1.

Comparison of the polarized intensity map of NGC 2976 with its Hα emission (Fig. 3) reveals that the PI distribution of the object is quite unusual compared to the other low-mass galaxies for which polarimetric observations were performed. Typically for dwarfs, the polarized signal is closely related to the regions where massive stars are formed. These findings were made in NGC 4449, where the emission follows a part of the massive arm that is actively forming stars (Chyży et al. 2000); IC10, in which only a polarized intensity near the giant H II regions was detected (Chyży et al. 2003; Heesen et al. 2011); NGC 1569, where multi-wavelength radio observations reveal PI features that are associated with Hα bubbles – outside the stellar disk (Kepley et al. 2010). However, in NGC 2976 the polarized emission mostly resides very far from H II regions. This is likely due to external agents (tidal interactions and perhaps ram pressure, see Sect. 4.5) and is, to some degree, also due to the Faraday depolarization. Faint Hα emission extends only to the west from the northern H II region and to the east from the central part of the system. Even trying to increase the signal-to-noise ratio in the Hα map by convolving it to the resolution of radio data does not reveal any extended emission[5]. This is in agreement with Thilker et al. (2007), where the galaxy was

[5] The same is true for the map in far-UV, which is also a tracer of star formation.

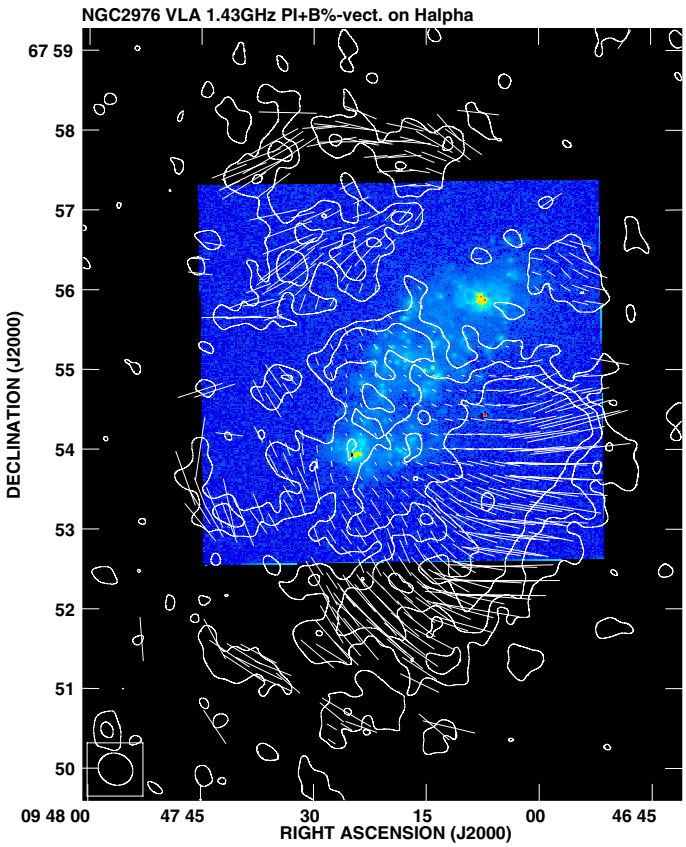

Fig. 3. Contours of polarized intensity and apparent B-vectors (not corrected for Faraday rotation) of polarization degree of NGC 2976 (obtained with Robust = 1 weighting) at 1.43 GHz superimposed on the Hα image (Dale et al. 2009). The contour levels are (3, 5, 8) × 9 (rms noise level) μJy/beam. A vector of 10″ length corresponds to the polarization degree of 12.5%. The map resolution is 26.8″ × 23.5″ HPBW, while the beam position angle is 62 degrees.

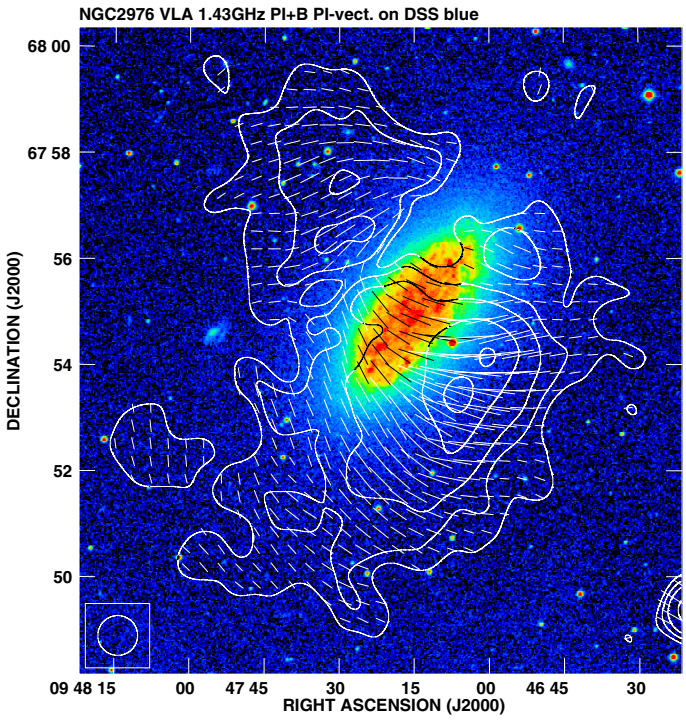

Fig. 4. Contours and apparent B-vectors (not corrected for Faraday rotation) of the polarized intensity of NGC 2976 at 1.43 GHz convolved to the resolution of 45″ and superimposed on the DSS blue image. The contour levels are (3, 5, 8, 16, 24) × 13 (rms noise level) μJy/beam. The vector of 10″ length corresponds to the polarized intensity of about 42 μJy/beam.

classified as not having an extended UV disk. While NGC 2976 shares a high level of optical symmetry with M 33, which also has a thin disk and a rotation that is only twice as fast (Tabatabaei et al. 2008), the polarized emission of NGC 2976 is much more asymmetric.

Based on the WSRT-SINGS survey, Heald et al. (2009) found that, in normal galaxies, their receding side is significantly depolarized at long wavelengths (of about 20 cm), owing to a geometry of large-scale magnetic fields and the longer way the polarized waves travel through the magneto-ionic medium. From the H I velocity field observations of NGC 2976 (publicly available within the THINGS survey, Walter et al. 2008) we found that the north-western part of the object has a receding major axis. This implies that this side of the galaxy should exhibit a less polarized emission, compared to the opposite side. This effect is actually observed for the optical disk.

The total power flux density measured at 1.43 GHz for NGC 2976 is 65.7 ± 2.8 mJy, while the polarized intensity flux density is 7.8 ± 0.8 mJy, which gives a total polarization degree of 12 ± 2%. Such values are typically observed in more massive spiral galaxies but at higher radio frequencies (e.g. Beck et al. 1996).

3.2. 4.85 and 8.35 GHz

In Fig. 5, the total power emission at 4.85 GHz from the Effelsberg telescope is presented (see also Jurusik et al. 2014). Its resolution is much lower (152″) than in the VLA observations. In this map, similarly to the high-resolution data, the TP signal has a maximum shifted to the northern part of the galaxy's disk, where one of the giant H II regions is located. The low-level emission of 1.35−2.25 mJy/beam is elongated in the NE direction (possibly it is not real). There is no such elongation to SE. A similar asymmetry was observed in the 1.43 GHz data (Fig. 1). The elongation in the NW direction seems to be correlated with a source that is also visible at 1.43 GHz. The total power flux density of NGC 2976 measured at 4.85 GHz is 30.0 ± 1.4 mJy (Table 3), which is in excellent agreement with the radio flux that is determined at the same frequency by Gregory & Condon (1991).

The morphology of polarized intensity at 4.85 GHz (Fig. 5) closely resembles that at 1.43 GHz. Here almost all (about 80%) of the polarized flux density, which is 1.6 ± 0.4 mJy (giving a polarization degree of about 5%, Table 3), comes from the southern part of the disk and the southern extension. Only some small polarized blobs have been detected in northern direction. The narrow emission from the disk is located close to the galaxy centre, while at 1.43 GHz it is barely shifted towards the south.

The noticeable difference in the polarized emission between 4.85 GHz and 1.43 GHz is related to the orientation of the B-vectors. At 4.85 GHz, the vectors are nearly perpendicular to those observed at the lower frequency. As the Faraday effects are smaller at shorter wavelengths, we can expect that the directions of B-vectors, which are observed at 4.85 GHz, are close to the intrinsic directions of magnetic field vectors (see Fig. 13).

The total power emission of NGC 2976 at 8.35 GHz is presented in Fig. 6. This is closely related to the optical disk. There is no radio emission extension to the NE direction seen at lower frequencies, as expected for steep-spectrum radiation (see Sect. 3.3). The total power flux density measured for this

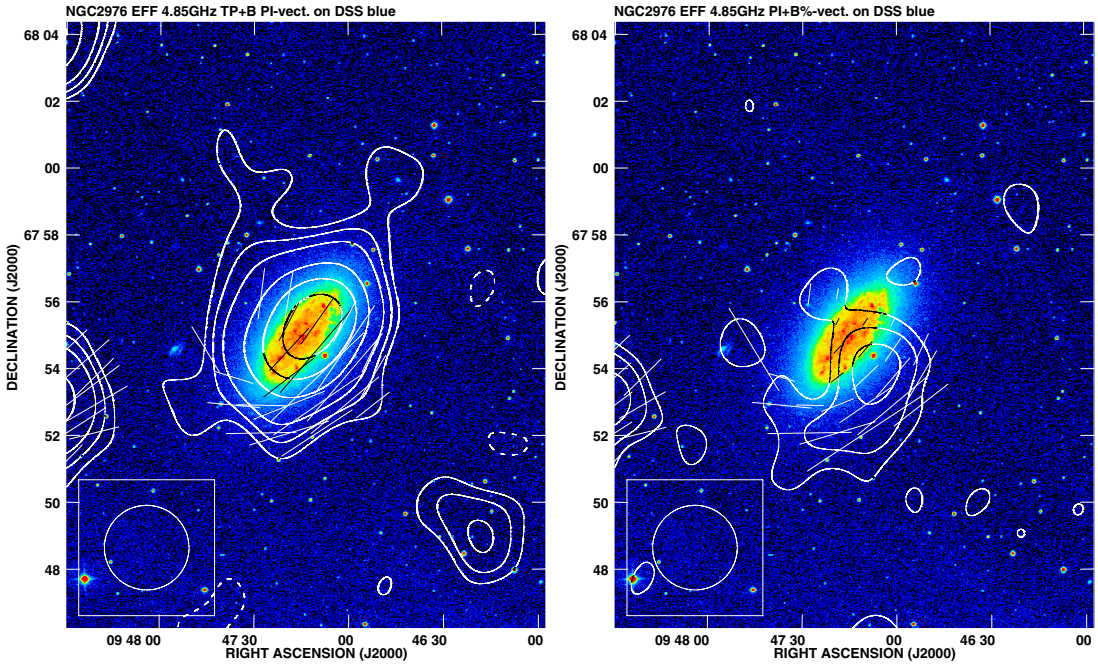

Fig. 5. *Left*: total-power contours and apparent B-vectors (not corrected for Faraday rotation) of polarized intensity of NGC 2976 at 4.85 GHz superimposed on the DSS blue image. The contours levels are (−5, −3, 3, 5, 8, 16, 24, 32) × 450 (rms noise level) μJy/beam. The vector of 10″ length corresponds to the polarized intensity of 33 μJy/beam. *Right*: contours of polarized intensity and apparent B-vectors (not corrected for Faraday rotation) of polarization degree of NGC 2976 at 4.85 GHz superimposed on the DSS blue image. The contour levels are (3, 5, 8) × 80 (rms noise level) μJy/beam. The vector of 10″ length corresponds to the polarization degree of 1.3%. The maps resolution is 152″ × 152″ HPBW.

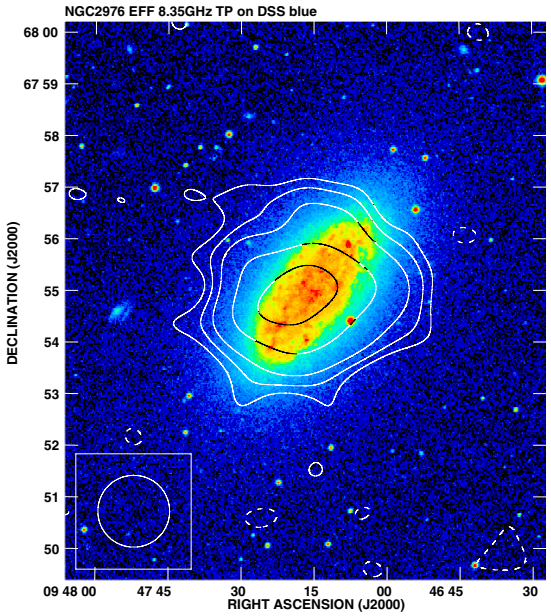

Fig. 6. Total-power contours of NGC 2976 at 8.35 GHz superimposed on the DSS blue image. The contours levels are (−5, −3, 3, 5, 8, 16, 24) × 230 (rms noise level) μJy/beam. The map resolution is 84″ × 84″ HPBW.

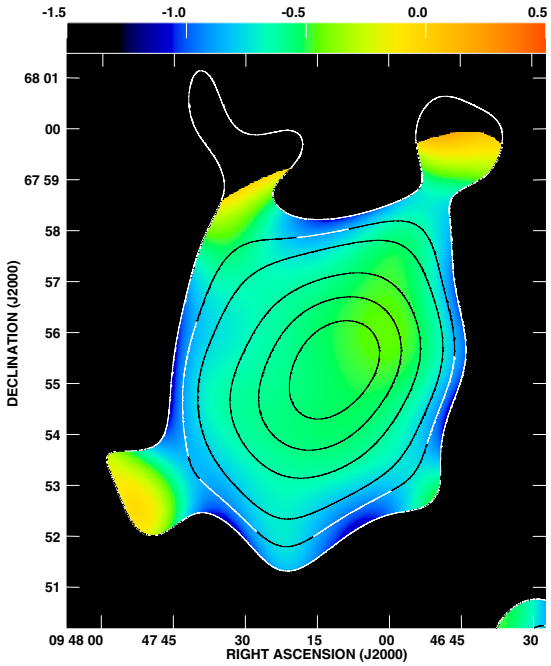

Fig. 7. Radio spectral index distribution between 4.85 and 1.43 GHz in NGC 2976 (colours). Both maps of total intensity were convolved to a common beam of 152″ (the beam is not shown). The contours represent the total power map at 4.85 GHz, their levels are: (−5, −3, 3, 5, 8, 16, 24, 32) × 450 (rms noise level) μJy/beam.

frequency is 19.3 ± 0.9 mJy (Table 3). In the polarization, we did not detect the galaxy. Probably weak weather artefacts or radio interference close to the noise level of the polarized intensity map prevented detection.

3.3. Spectral index distribution

The map of spectral index distribution shown in Fig. 7 was computed for NGC 2976 using the maps at 1.43 GHz and 4.85 GHz, after convolving them to a common resolution. The input maps were cut at 3 × rms noise level. The uncertainty of the obtained values is less than 0.4. Despite the low resolution of the map, one of the large H II regions in the northern part of the disk, where the spectral index reaches a level as high as −0.4, −0.5, is visible. In the rest of the disk, the spectral index of about −0.6, −0.7

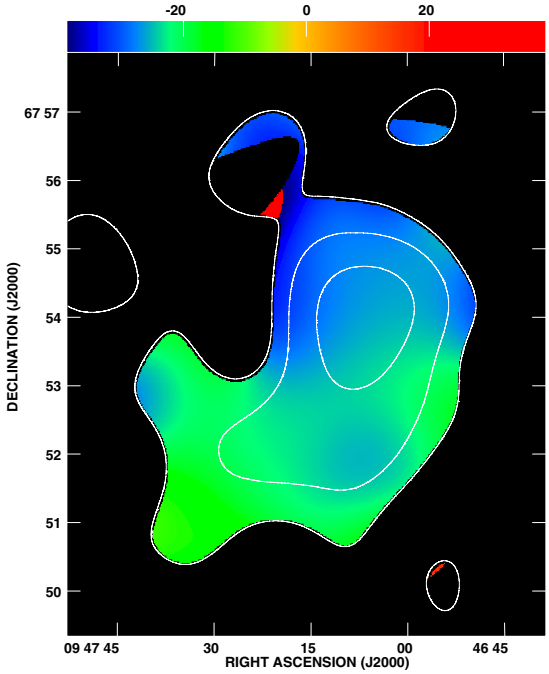

Fig. 8. Distribution of Faraday rotation measure (in rad m^{-2}, not corrected for the foreground RM) from the data at 4.85 and 1.43 GHz in NGC 2976 (colours). The contours represent the polarized intensity map at 4.85 GHz, the levels are: (3, 5, 8) × 80 (rms noise level) μJy/beam. The map resolution is 152″.

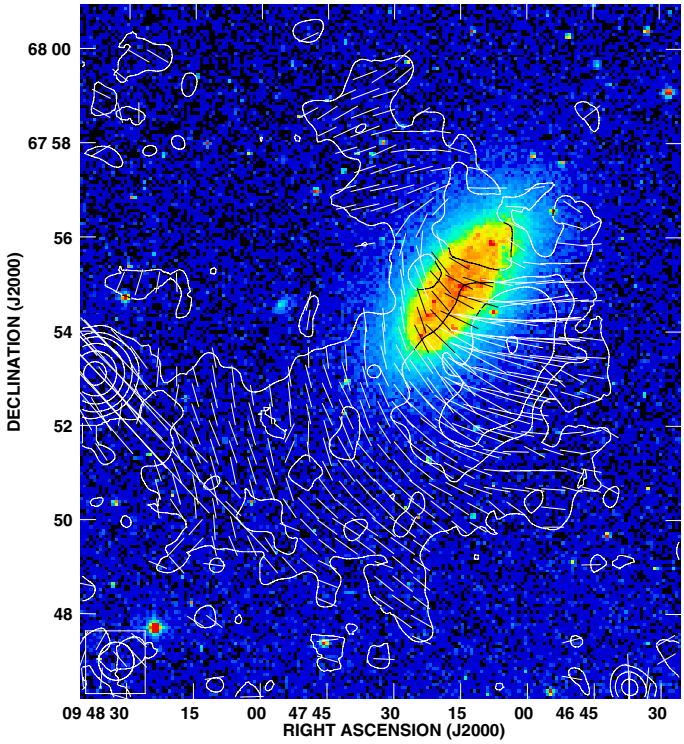

Fig. 9. Contours and apparent B-vectors (not corrected for Faraday rotation) of polarized intensity of NGC 2976 from the WSRT-SINGS data superimposed on the DSS blue image. The contour levels are (3, 5, 8, 16, 32, 64) × 25 (rms noise level) μJy/beam. The vector of 10″ length corresponds to the polarized intensity of about 31.3 μJy/beam. The map resolution is 48.6″ × 45.0″ HPBW.

is observed. These values are normally encountered in the spiral arms of galaxies (see, e.g. Chyży et al. 2007b). This could mean that the emission from the optical disk is dominated by the radiation of young relativistic electrons that are spiralling in a magnetic field with some small contribution from thermal emission (see Sect. 4.1). Outside the disk, the spectrum steepens sharply, reaching values of about −0.9, apparently owing to the aging of relativistic particles there. By way of an example, a similar effect was found for NGC 1569 (Kepley et al. 2010).

3.4. Distribution of rotation measure

In Fig. 8, the distribution of rotation measure (with uncertainty less than 6 rad m^{-2}) is shown. It was calculated in a "classic" way on a pixel-by-pixel basis for the signal-to-noise ratio that was greater than 3, using the polarization angle maps available at two frequencies of 1.43 and 4.85 GHz. We note from this map that the rotation measure observed for NGC 2976 is mostly negative. The values of RM change smoothly from the north to the south-western direction. In the northern part of the object, RM has a value of about −35 rad m^{-2}. In moving to the south, the rotation measure grows from −30 to −23 rad m^{-2}, taking a value of about −13 rad m^{-2} in the galaxy's SE part.

When analysing the data on the rotation measure, the contribution from the Milky Way should be taken into account. One of the most standard ways to determine this contribution consists of using some nearby polarized background sources. In the case of NGC 2976, a suitable source is located at RA (J2000.0): $09^h48^m35^s$, Dec(J2000.0): 67°53′10″. Assuming that its internal RM is negligible, the foreground rotation measure for this source is about −35 rad m^{-2}. This is in excellent agreement with the foreground rotation measure in the direction of NGC 2976 that is reported by Heald et al. (2009), based on their WSRT-SINGS data. This foreground RM also agrees with the all-sky map published by Johnston-Hollitt et al. (2004).

Thus, taking into account the Milky Way rotation measure, it seems the magnetic field directed towards the observer can actually be seen within NGC 2976. After correcting for the foreground RM, it ranges from zero in the north to +22 rad m^{-2} in the south-east. These values are almost an order of magnitude lower than the rotation measures typically observed in normal galaxies at high frequencies (of about ±100 rad m^{-2}, Beck & Wielebinski 2013) and some dwarf galaxies, e.g. NGC 4449 (Chyży et al. 2000) and NGC 1569 (Kepley et al. 2010). The rather low value of rotation measure found in NGC 2976 could imply that the regular magnetic fields are weak in the object. Other possible explanations are that there is a low content of thermal electrons (which also affect the rotation measure) in the regions from which polarized intensity comes, or that the magnetic field in NGC 2976 is aligned mainly in the sky plane.

3.5. RM synthesis

For NGC 2976, spectro-polarimetric observations with the WSRT were also performed and analysed using the RM synthesis method (Heald et al. 2009) but with high spatial resolution and low sensitivity to extended radio structures. After re-imaging these data (see Sect. 2.3 for details), it was possible to discover polarized intensity structures (Fig. 9), which had not been seen previously by Heald et al. (2009). A comparison of the new WSRT-SINGS and VLA (see Fig. 4) polarized intensity images reveals that the distributions of PI in both the datasets are in very close agreement. As in the VLA, a characteristic southern bright PI region and an extension to the north are also visible in the WSRT image. Furthermore, these data confirm the existence of the polarized emission in the SE direction, which was seen

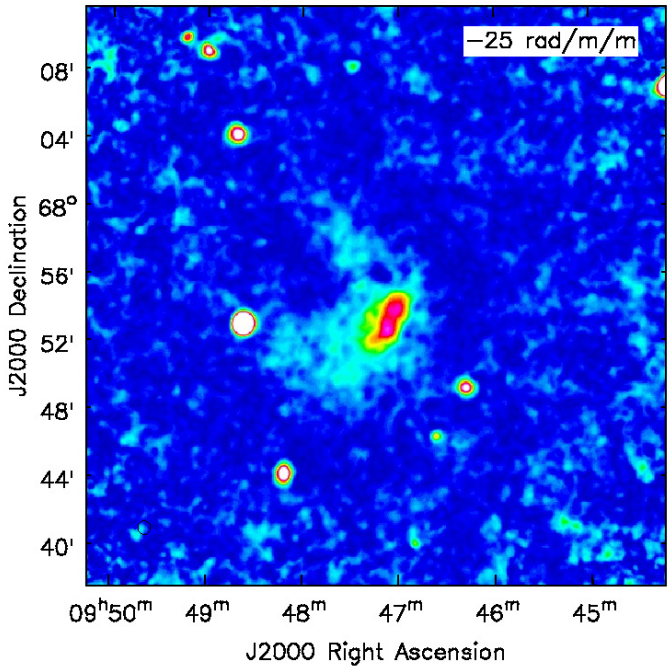

Fig. 10. The particular Faraday depth of −25 rad m^{-2}, for which most of polarized emission from NGC 2976 was detected. Note the twice as large scale of the image than that presented in Fig. 9.

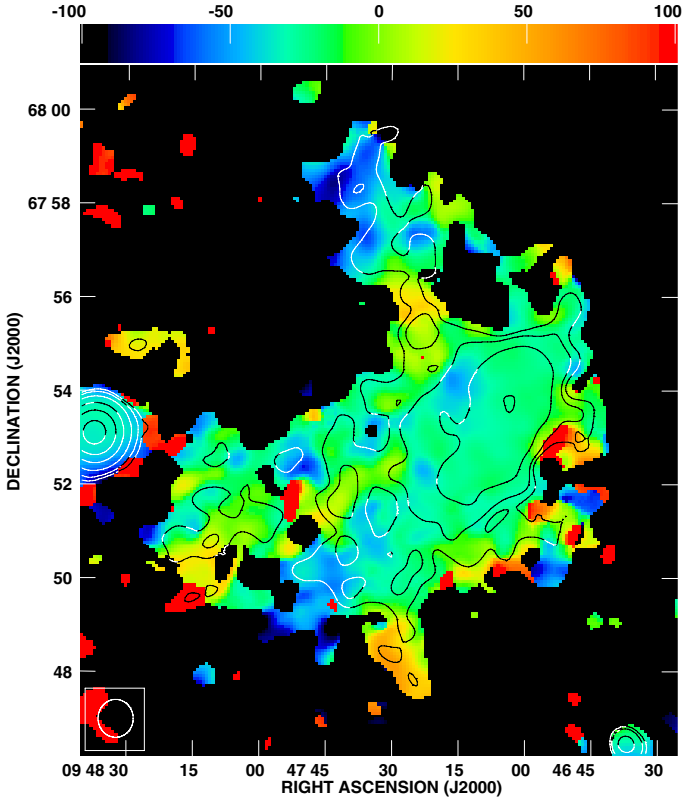

Fig. 11. Distribution of Faraday depths (in rad m^{-2}) for the maximum of polarized intensity signal for NGC 2976 (see text for details). The contour levels representing the polarized intensity are: (4, 5, 8, 16, 32, 64) × 25 (rms noise level) μJy/beam. The map resolution is 48.6″ × 45.0″ HPBW.

after a convolution of the VLA image to the lower resolution of 45″. Compared to the PI emission, the orientations of B-vectors also agree well between both the observations[6].

Scanning through the RM cube along the Faraday depth reveals that the polarized emission coming from NGC 2976 is mostly point-like in this domain. This is in agreement with the findings of Heald et al. (2009). In Fig. 10, the slice from the cube at the depth of −25 rad m^{-2} is shown, where most of detected polarized signal can be seen.

Taking into account that there is only one point-like Faraday component in the cube, it was possible to construct a maximum Faraday depth map for the object (Fig. 11, Sect. 2.3). The distribution of Faraday depths, as shown in the image, was cut off at the 3 × rms (of 25 μJy/beam) noise level of the PI map. We note that, according to Brentjens & de Bruyn (2005), a total signal-to-noise ratio greater than 4 is needed to determine reliable information about Faraday depth using the RM Synthesis method. This limit is indicated in the image by the first PI contour. A comparison of the high resolution (48.6″ × 45″) maximum Faraday depth map that was obtained by applying the RM synthesis technique to the low resolution RM map (Fig. 8) obtained by the "classical method" shows that they are similar. Particularly noticeable are the negative Faraday depths found in the strongly polarized SW region (this region shows a Faraday depth of about −25 rad m^{-2}). In the northern, south-eastern, and western parts of the galaxy, where the signal-to-noise ratio is lower, the maximum Faraday depth distribution is more chaotic. The similarity of both the maximum Faraday depth and RM maps indicates that Faraday depolarization is relatively small – around 1 GHz in NGC 2976.

[6] The central frequencies between the datasets differ slightly; for WSRT, it is about 1.5 GHz, while for VLA, it is 1.43 GHz, so the B-vectors orientations are actually slightly different.

4. Discussion

4.1. Thermal fraction

The radio emission of normal galaxies has thermal and non-thermal components. To be able to estimate the magnetic field strength, which is directly related to the non-thermal radio emission, both these components must first be properly separated. The best method to separate them consists of fitting a simple model of a thin optical disk to the multifrequency radio data (Niklas et al. 1997). The model is described by the following equation:

$$\left(\frac{S_\nu}{S_{\nu_0}}\right) = f_{\rm th}(\nu_0)\left(\frac{\nu}{\nu_0}\right)^{-0.1} + (1 - f_{\rm th}(\nu_0))\left(\frac{\nu}{\nu_0}\right)^{\alpha_{\rm nth}}, \quad (1)$$

where S_ν and S_{ν_0} are radio fluxes for a given frequency and the frequency for which the separation is performed. Here, $f_{\rm th}(\nu_0)$ is the so-called thermal fraction, being a ratio of thermal and total radio fluxes, and $\alpha_{\rm nth}$ is the non-thermal spectral index. For the thermal emission, a spectral index of −0.1 is assumed. In the case of NGC 2976, it was possible to use this method taking flux values from our observations at three frequencies. Moreover, as it was pointed out in Sect. 3, this galaxy was also observed in the 2.8 cm survey of Shapley-Ames galaxies (Niklas et al. 1995). Thus, four measurement points (Fig. 12) are available, which is a minimum that enables us to fit the above model and get the desired thermal fraction and non-thermal spectral index. The thermal fraction obtained in this way $f_{\rm th}$ is 0.16+/−0.12 at 1.43 GHz, while $\alpha_{\rm nth}$ is −0.82+/−0.20. However, we note that the highest frequency data point in the spectrum (from Niklas et al.) seems

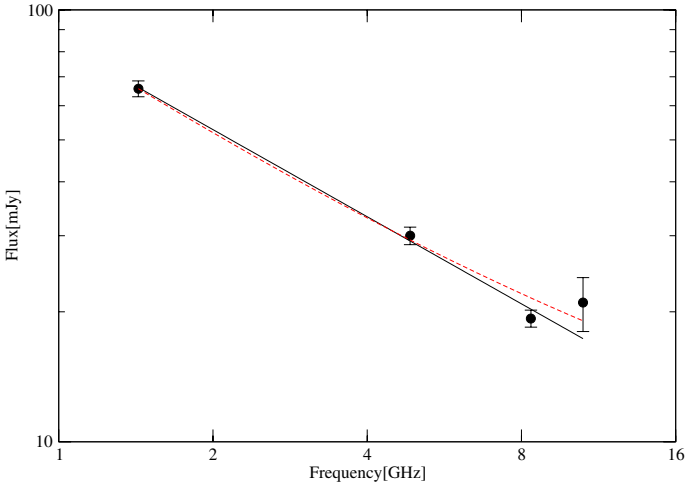

Fig. 12. Radio spectrum of NGC 2976. The point at the highest frequency is from Niklas et al. (1995). The solid black line represents a power-law model fitted to the data. The red dashed line represents the fitted model of a thin disk in which $f_{\rm th} = 0.16$ and $\alpha_{\rm nth} = -0.82$ (see text for details).

to be shifted upwards from the fit and should be regarded with caution.

An alternative method of separation of thermal and non-thermal emission consists of estimating the thermal radio flux using star formation tracers, for instance, Hα emission (see, e.g. Niklas et al. 1997; Chyży et al. 2007a). It should be stressed, however, that Hα is affected by internal extinction, which is usually barely known about (if at all), and which makes this method less effective. The extinction uncertainty is more problematic for large well-evolved spiral galaxies than for low-metallicity dwarfs. According to the recent studies, it is possible to estimate this effect by also taking into account data on infrared emission (Calzetti et al. 2007; Kennicutt & Evans 2012). By inserting the Hα and infrared emission into the classical formula of the thermal flux estimation (Niklas et al. 1997), we obtained the radio thermal flux at frequency ν (see also, Jurusik et al. 2014):

$$S_\nu[\mathrm{mJy}] = 2.238\times10^9\left(\frac{S_{\mathrm{H}\alpha}+0.020\nu_{\rm IR}S_{\rm IR}}{\mathrm{erg\ s^{-1}\ cm^{-2}}}\right)\times\left(\frac{T_{\rm e}}{\mathrm{K}}\right)^{0.42}\times\left[\ln\left(\frac{0.04995}{\nu[\mathrm{GHz}]}\right)+1.5\ln\left(\frac{T_{\rm e}}{\mathrm{K}}\right)\right], \quad (2)$$

where $S_{\mathrm{H}\alpha}$ and $\nu_{\rm IR}S_{\rm IR}$ are Hα and IR (multiplied by the IR frequency) fluxes, respectively. For NGC 2976, the Hα flux was taken from Kennicutt et al. (2008), while the IR 24 μ flux was taken from the *Spitzer* satellite observations (Dale et al. 2009). Here, $T_{\rm e}$ was assumed to be 10^4 K. The thermal fraction obtained in this way is 0.17 ± 0.02 at 1.43 GHz, which is in excellent agreement with the results of the fitting method.

This is quite unexpected, since these thermal fractions and non-thermal spectral indices are typically observed for normal spiral galaxies that are much more massive than NGC 2976. Niklas et al. (1997) determined the mean $f_{\rm th}$ of 0.08 ± 0.01 (at 1 GHz) and an average $\alpha_{\rm nth}$ of −0.83 ± 0.02 for a sample of 74 galaxies of various morphological type. For the dwarfs, much higher thermal fractions were found; Chyży et al. (2003) estimated that for IC 10 $f_{\rm th}$ reaches a level of 0.6 (see also, Heesen et al. 2011) and for NGC 6822, it is even as high as 0.8−0.9 at 10.45 GHz (the thermal fraction of NGC 2976 at this frequency would only be about 0.45). Even higher $f_{\rm th}$ were obtained for three late-type galaxies that are characterized by low star formation activity and explained by their weak magnetic fields and nonlinear dependency between nonthermal emission and SFR (Chyży et al. 2007a).

In the same way as the thermal fraction, the global spectral index of NGC 2976 (−0.67 ± 0.03) also follows the value of −0.74 ± 0.12 found for a sample of normal galaxies (Gioia et al. 1982).

4.2. Magnetic field strength

After separating the thermal and non-thermal emissions, it was possible to estimate the strength of the magnetic field in the investigated object. The formulas given by Beck & Krause (2005) were used for this purpose, with the assumption of an energy-density equipartition between the total field and cosmic rays (CR). A typical disk thickness (corrected for the projection effects) of 1 kpc and the proton-to-electron ratio of 100 were assumed in the calculations (using the non-thermal spectral index of 0.83 from Niklas et al. 1997). The mean non-thermal surface brightness was measured in the area that was determined by the requirement of radio emission being at a level of at least 3σ noise level at 1.43 GHz (see Sect. 3), giving the total magnetic field strength $B_{\rm tot}$ of 6.6 ± 1.8 μG.

The total magnetic field strength obtained is higher than the mean value of <4.2 ± 1.8 μG found for a sample of Local Group dwarfs (Chyży et al. 2011), but lower than the average value of 9 ± 2 μG that was estimated for a sample of 74 galaxies of various morphological types (Niklas 1995). However, we note that the Niklas sample also included interacting objects, which are usually characterized by higher magnetic fields strengths than those in normal galaxies (Drzazga et al. 2011). In spiral galaxies with moderate star formation activity, e.g. in M 31 and M 33, and so more similar in this sense to NGC 2976 (for which $SFR \approx 0.12\ M_\odot$/yr, see Table 1), the field strengths of only about 6 μG were found (Beck & Wielebinski 2013).

Another important parameter to describe galactic magnetic field properties is the degree of field order, defined as a ratio of the ordered ($B_{\rm ord}$) and random ($B_{\rm ran}$) magnetic field components. This is a useful measure of the net production of the ordered field. The $B_{\rm ord}$ estimated from the data about polarized flux (using formulas of Beck & Krause 2005) for NGC 2976 is 2.8 ± 0.8 μG. This is a typical value for the spirals, in which ordered fields in the range of 1−5 μG are observed (Beck & Wielebinski 2013). Along with the random field component (which for NGC 2976 is $B_{\rm ran} = 6.0 \pm 1.6\,\mu$G), this gives a very high value of degree of field order of 0.46 ± 0.17. Consequently, with respect to the strength of magnetic field components, NGC 2976 resembles well-defined spiral galaxies rather than dwarfs.

4.3. Generation of magnetic field

As was shown in Sect. 3, non-zero rotation measures were found for NGC 2976, which possibly suggest that this object hosts a large-scale partially regular magnetic field. One of the mechanisms to explain the generation of this field is a large-scale magnetohydrodynamic dynamo (e.g. Widrow 2002). To investigate if this process is at work in this galaxy, we can estimate its efficiency, usually described by a dynamo number (Shukurov 2007)

$$D \approx 9\frac{h_0^2}{u_0^2}s\omega\frac{\partial\omega}{\partial s}, \quad (3)$$

where, h_0 is the vertical-scale height of the galactic disk, u_0 is the velocity of turbulent motions, s is the radial distance from the centre of the galaxy, ω is the angular velocity and $s\frac{\partial\omega}{\partial s}$ is the shear rate. To estimate this number for NGC 2976, we assumed a scale height of 0.5 kpc, typical for dwarf galaxies (e.g. Chyży et al. 2011) and u_0 from H I observations of 11 km s^{-1} (Stil & Israel 2002b). The dynamo number was computed for a radius of 2.0 kpc, within which the rotation curve can be approximated as flat (as it was suggested by Stil & Israel 2002b, but questioned by de Blok et al. 2008). At this distance, the rotation velocity reaches a value of about 71 km s^{-1} (Stil & Israel 2002b). Although it rotates with a velocity that is somewhat slower than that of typical spirals it is still faster than the low-mass galaxies, NGC 4449 and the SMC (50 and 60 km s^{-1}, respectively). As the rotation of the disk in NGC 2976 is also more regular than in SMC and NGC 4449, it can be expected that the large-scale dynamo process can operate in this object.

Indeed, an estimation for NGC 2976 of a shear rate of about 36 km s^{-1} kpc^{-1} and the absolute value of the dynamo number of about 23 shows that this is comparable to the dynamo number that was obtained for the Milky Way (of about 20) at the distance of the Sun (Shukurov 2007). It exceeds the critical limit $|D_{\rm critical}| \sim 8-10$, below which the large-scale dynamo is inefficient (Shukurov 2007). This value does not seem to be typical for dwarf galaxies, for which mostly subcritical dynamo numbers have been obtained (Chyży et al. 2011; Mao et al. 2008). Even for the Large Magellanic Cloud, which is much larger and more massive than NGC 2976, Mao et al. (2012) estimated $|D|$ as ∼10 only. Thus, with the linear size of about 6 kpc and H I mass of $1.5\times10^8\,M_\odot$ (Stil & Israel 2002a, Table 1), NGC 2976 is several times less massive than SMC and NGC 4449 and could set the lowest mass threshold for a large-scale dynamo to work.

Based on simple estimates for the turbulence transport coefficients, it has often been argued for a too long growth time of the $\alpha-\omega$ dynamo (see e.g. Shukurov 2007). But direct simulations of the turbulent ISM by Gressel et al. (2008) led to growth times of approximately 200 Myr for an $\alpha-\omega$ dynamo process. A similar growth time is found by Hanasz et al. (2004) with cosmic ray-driven steering of the ISM. In this type of dynamo process, supernova explosions produce cosmic rays, the pressure from which leads to the increased efficiency of the α effect, which is responsible for generating the poloidal component of magnetic field. It has recently been successfully applied in simulations of magnetic fields in spiral (Hanasz et al. 2009) and barred galaxies (Kulpa-Dybeł et al. 2011), yielding dynamo growth timescales of 270 Myr and 300 Myr, respectively. The CR dynamo is also considered to be a particularly attractive mechanism for dwarfs, and is able to account for their regular magnetic fields (Gaensler et al. 2005; Kepley et al. 2010; Mao et al. 2012). This explanation is further supported by recent global numerical simulations of dwarfs performed by Siejkowski (2012), who find that the magnetic field can be amplified in low-mass objects only if their rotational velocity exceeds 40 km s^{-1}, However, a velocity of at least 60 km s^{-1} is needed for the efficient generation of a magnetic field, and for such fast rotators, their dynamo action depends mainly on rotational velocity.

By confronting the maximum rotational velocity of NGC 2976 with these results, we can see that the cosmic-ray driven dynamo is actually able to operate efficiently in this object with e-folding amplification time not greater than 400 Myr (cf. Siejkowski's models with $v_{\rm rot} \geq 60$ km s^{-1}). Furthermore, the strength of the magnetic field in NGC 2976 (Sect. 4.2) is roughly in agreement with the simulations, where for the fast rotating models this is at the level of a few μG.

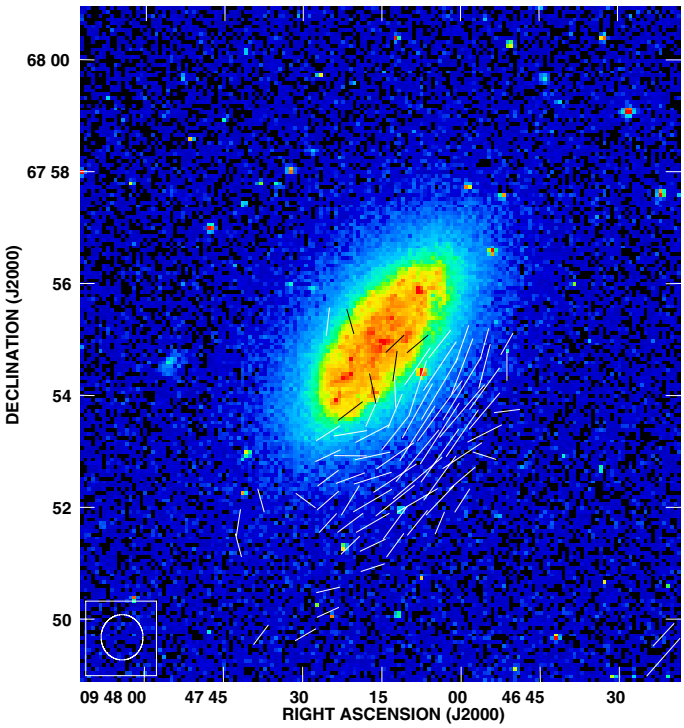

Fig. 13. Orientations of intrinsic magnetic field vectors (plotted for a signal-to-noise ratio of at least 5 in PI) for NGC 2976 from the reprocessed WSRT-SINGS data superimposed on the DSS blue image. The vector of 10 length corresponds to the polarized intensity of 50 μJy/beam. The beam size is 48.6 × 45.0 HPBW.

4.4. Magnetic field morphology of NGC 2976

Apart from the field strength, its morphology is also crucial when discussing the large-scale dynamo process. In Fig. 13, a distribution of magnetic field orientations (B-vectors corrected for Faraday rotation) is presented for NGC 2976. The map was computed only for the regions where signal-to-noise ratio was high enough (see Brentjens & de Bruyn 2005). The most surprising are the almost azimuthal (pitch angle around zero degrees) directions of the field in the southern part of the object, where the maximum of polarized intensity is observed. Hence, we suspect that the magnetic field in NGC 2976 could not have been generated by the galactic-scale dynamo action alone, since a spiral morphology of magnetic fields would have arisen as a result. So far, this kind of field has been observed most clearly in the ring galaxy NGC 4736 (Chyży & Buta 2008), which does not exhibit any strong density waves, like NGC 2976. The nearly azimuthal magnetic field in the south, along with the enhanced polarized intensity and no corresponding enhancement of total power emission (cf. Figs. 1 and 3) imply a field compression in this part of the galaxy. The degree of field order of 114 ± 48% that is estimated for this area is very high, since it is 2.5 times higher than the average value (Sect. 4.2).

4.5. Tidal interactions or ram pressure?

Ram pressure caused by the intra-group medium of the M 81 galaxy group is one possibility of accounting for the magnetic field structure of NGC 2976. This mechanism is most often observed in clusters of galaxies, e.g. in the Virgo cluster (see, e.g. Vollmer et al. 2013). In galaxy groups, the relative speed of objects with respect to the surrounding medium and its density (the

quantities that the ram pressure depends on) are usually one order of magnitude lower than for the clusters. Recently, Bureau & Carignan (2002) have considered the influence of ram pressure on the galaxy HoII, which is located about 0.5 Mpc from the core of the M 81 group. They argue that, for this low-mass object, the density of the ambient medium of the M 81 group and its relative velocity are high enough to cause its gas stripping. Thus, Bureau & Carignan's argument is all the more valid for NGC 2976, the distance of which to the group centre is lower (and was supposedly even more so, in the past). The ram pressure affects only the gaseous component (hence the magnetic field frozen into the plasma), leaving the stellar disk untouched. In the polarized emission, a compressed field is usually observed at the windward side, forming a polarized ridge and a diffuse extension in the opposite side of galactic disk (see, e.g. Vollmer et al. 2010, 2013). This kind of effect could explain the case of NGC 2976 since, in fact, the structure of its magnetic field closely resembles those observed in some Virgo cluster spirals, particularly in NGC 4501 (Vollmer et al. 2008), which has a similar inclination to the galaxy in question.

However, for the ram pressure, a more narrow shock front is to be expected and not a wide one, as observed in the investigated object. Compared to NGC 4501, the polarized emission in NGC 2976 is extended farther beyond the optical disc. Also, no index flattening is seen in NGC 2976 (Sect. 3.3) in the region of maximum polarized emission, which is expected for the strong ram pressure (see Vollmer et al. 2013). Moreover, recent studies of nearby low-mass galaxies show that NGC 2976 fits into the general trend of radio-infrared correlation that is determined for more massive spirals (Jurusik et al. 2014). For Virgo cluster galaxies that exhibit ram pressure stripping, deviations from the correlation were observed (Murphy et al. 2009; Vollmer et al. 2013), which can be accounted for by an enhanced radio emission owing to gas compression. Thus, again, in the case of NGC 2976, the ram pressure effects, if any, must be weak. Also the morphology of neutral hydrogen in the southern part of NGC 2976, while being coincident with the PI maximum, it is not so clearly defined as in the other galaxies that are known to have been stripped, e.g. in the Virgo spirals, NGC 4501 (Vollmer et al. 2008) and NGC 4654 (Soida et al. 2006). Even the gas compression in HoII (Bureau & Carignan 2002) seems to be more pronounced than in NGC 2976. Taking the present location of NGC 2976 into account with respect to the group core, it is quite plausible that this object has already passed the peak of ram pressure. In fact, Otmianowska-Mazur & Vollmer (2003) define two phases that are related to ram pressure, i.e. a compression phase and a phase of re-accretion, when gas falls back onto the galactic disk in a spiral-like manner. In their simulations, in the early stages of gas re-accretion the polarized intensity is also enhanced. Moreover, maxima of the gas distribution outside of the disk should occur in this phase, which is actually observed in the case of NGC 2976. Another possibility, related to the ram pressure, is the influence of draping flows which modify the large-scale dynamo action and lead to an asymmetric PI distribution (Moss et al. 2012). However, in this case, relatively strong ram pressure is also needed.

These potential difficulties with the ram pressure scenario suggest that, in NGC 2976, tidal interaction could play a major role. It is thought that the galaxy could have been influenced by M 81 in the past, during its passage close to the group centre. At present, NGC 2976 is located south-west of the M 81 group's core. This kind of interaction, between M 81 and NGC 2976, could have occurred more than 1.3 Gyr ago, as has been approximately estimated by Williams et al. (2010). In

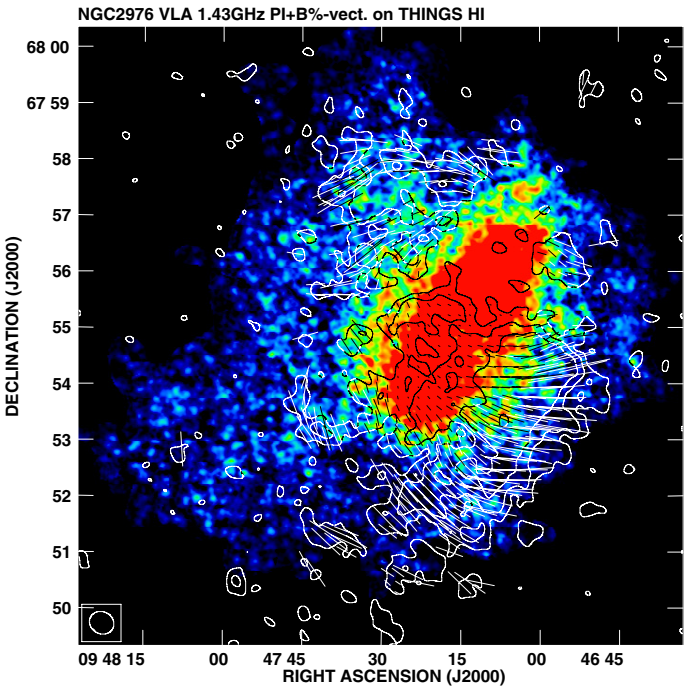

Fig. 14. Contours of polarized intensity and apparent B-vectors (not corrected for Faraday rotation) of polarization degree of NGC 2976 at 1.43 GHz (obtained with Robust = 1 weighting) superimposed on the H I map (from the THINGS survey, Walter et al. 2008). The contour levels are (3, 5, 8) × 9 (rms noise level) μJy/beam. The vector of 10″ length corresponds to the polarization degree of 12.5%. The polarized intensity map resolution is 26.8″ × 23.5″ HPBW (the beam position angle is 62 degrees). The H I map resolution is 7.4″ × 6.4″ HPBW (the beam position angle is 72 degrees).

the high-sensitivity maps of distribution of neutral hydrogen, a long strip of H I that connects the object with the group centre, was detected (Chynoweth et al. 2008). Hence, some tidal interactions actually could have taken place (Appleton et al. 1981; Appleton & van der Hulst 1988; Chynoweth et al. 2008). The tidal origin of the magnetic field morphology, which is observed in NGC 2976, explains its asymmetric PI distribution, seen at 1.43 GHz and 4.85 GHz and the location of the polarized emission beyond the optical disk and well within the H I distribution (Fig. 14). The galaxy also seems not to have a strong ordered magnetic field in its disk. Altogether, these observables have been recognized by Vollmer et al. (2013) as signatures of tidal interactions in the Virgo cluster spirals.

Usually, the degree of field order is regarded as an indicator of tidal interactions, since it is statistically lower for the interacting objects than for the non-interacting ones (Drzazga et al. 2011). This is not the case for NGC 2976, for which the degree of field order mentioned above (Sect. 4.2) has a value that is typically found in non-interacting galaxies. This is not too surprising, since obviously interacting galaxies are known about, e.g. NGC 4254, for which the degree of field order is similar to those observed in normal objects (Chyży 2008).

However, there are also some problems with attributing the unusual structure of the magnetic field of NGC 2976 to tidal forces. One of them is its ideally symmetric stellar disk and halo, which can be an apparent indication that the galaxy has not been disturbed for a long time (Bronkalla et al. 1992). This makes the tidal interactions scenario more doubtful, but not impossible, since magnetic structures can involve quite a long "memory" of past events (from even 1 Gyr, see Soida et al. 2002 and references therein). This memory is longer when compared to

the other components of the ISM and the stars. The best example of a mismatch between the structure of the stellar disk and the structure of the field was so far found in the flocculent galaxy, NGC 4414 (Soida et al. 2002). In this high-mass and non-interacting object, as in NGC 2976, a symmetric flocculent disk can be seen, suggesting that it has not been strongly affected recently. However, the magnetic field contradicts this altogether, since it shows a complicated morphology as well as a strong RM jump in the southern part of the object, which is not expected in a non-disturbed galaxies (Soida et al. 2002). Indeed, recent studies of de Blok et al. (2014) indicate that NGC 4414 could have taken part in a minor interaction with low mass galaxy in the past.

From the discussion presented above, we can propose the following scenario, which reasonably explains the structure of the magnetic field in NGC 2976. More than 1 Gyr ago, the galaxy took part in gravitational interactions between galaxies in the group centre. At this time, tidally induced radial inflow of gas occurred, leading to the outside-in truncation of star formation, specifically for NGC 2976 (Williams et al. 2010). As shearing motions and compression are both associated with gas inflow, hence like ram pressure, they are able to produce an ordered or anisotropic magnetic field from its random component, while not disturbing the stellar disk. These external influences were probably relatively weak, and thus could have had more impact on the least dense ISM phases. The currently observed anomalies in the magnetic field configuration of the object would be a result of the "memory" of these past interaction events.

Williams et al. (2010) also consider that the ram pressure effect causing the stripping of halo gas as an alternative (or additional process), which is able to explain the star formation history of NGC 2976. From our studies presented above, it seems that this scenario is less likely than the gas redistribution owing to tidal interactions. However, we cannot exclude that ram pressure in its late phase of H I gas and magnetized plasma reaccretion could also have played some part in shaping the magnetic field in this object.

Detailed 3D numerical MHD simulations are required to evaluate this scenario. NGC 2976 is a quite suitable object for this type of simulation, since it does not exhibit any strong density waves to influence the structure of its magnetic field. Moreover, from the observational point of view, sensitive X-ray data are needed to detect the hot gas halo around this object. This kind of halo, if any, could have a significant impact on the effectiveness of the ram pressure process in NGC 2976.

4.6. Pure disk dwarf galaxies as a potential sources of IGM magnetic fields

The magnetization of intergalactic space is still an open problem in modern astrophysics (see Sect. 1). As it was shown in Sect. 3, NGC 2976 exhibits a strong TP radio emission, extending up to 4.5 kpc (without correction for the inclination angle), thus in a general agreement with Chyży et al. (2011) predictions that are based on the assumption that the star formation was continuous in galaxies, which is the case for NGC 2976 (Williams et al. 2010). While it is not sufficient to regard NGC 2976 as an effective provider of magnetic field into the IGM, it is worthwhile noting that this galaxy shows also an extended polarized emission of a similar extension as the total power one (5 kpc, if measured in the higher sensitivity map, Fig. 4). Thus, apart from the random component of the magnetic field, NGC 2976 can also supply well-ordered fields to the IGM, at least within its closest neighbourhood. Moreover, the calculations presented above show that this object is not only able to host a large-scale dynamo, but also creates favourable conditions for it to act at a level that is typically found in spiral galaxies. This, along with its low mass, makes NGC 2976 one of the best known instances of providers of a regular (not just ordered) intergalactic magnetic field. Even in the galaxy NGC 1569, of an H I mass similar to NGC 2976, with a huge radio halo that extends up to 4 kpc (as estimated in Fig. 1 from Kepley et al. 2010), no highly polarized signal was detected at 1.4 GHz (at higher frequencies, a stronger PI is visible, but it is less extended). Therefore, this object is as efficient as NGC 2976 in providing random fields to its neighbourhood, but it is much less efficient in providing ordered and regular fields.

Hence, to efficiently magnetize the whole M 81 group with a radius of about 211 kpc (Karachentsev 2005), or at least its central part, more objects from the pure disk dwarf class are needed. However, finding objects like NGC 2976 is difficult because its morphology seems to be unique. It does not look like any other known nearby galaxy, featuring a bright sharply-edged disk, which is perhaps just a short-lived stage within its entire evolution (Williams et al. 2010). In fact, within the M 81 group, which consists of 29 galaxies (Karachentsev 2005; or 36 according to Karachentsev & Kaisin 2007), only one galaxy can be found that is similar to NGC 2976, i.e. NGC 4605 (Karachentsev & Kaisin 2007). This galaxy also has a well-defined stellar disk and is only slightly larger (with its disk of about 8 kpc) than NGC 2976[7]. In short, the small number of the galaxies of this type makes their significant role for the group's magnetization process rather doubtful. It should be emphasised here that this conclusion is based only on the observed 1.43 GHz radio envelope. If we assume that the magnetic field of NGC 2976 extends to at least a distance where its H I emission is visible (Chynoweth et al. 2008), the volume which the object could effectively magnetize would be much larger. To detect the full envelope of synchrotron emission that is related to this type of field, a new generation of radio telescopes are needed. LOFAR is one of the best-suited instruments for this task since it can observe at low frequencies within the range of 30−240 MHz. Thus, it would be able to detect a weak magnetic field that is highlighted by low-energy electrons leaving the disk of NGC 2976.

5. Summary and conclusions

For NGC 2976, a pure-disk dwarf galaxy, deep polarimetric observations at 1.43 GHz, 4.85 and 8.35 GHz were performed and then supplemented with re-imaged WSRT-SINGS data. The radio images that were obtained were compared with data in other spectral domains, which led to the following conclusions:

- A large total-power and polarized radio envelope surrounding the object was discovered.
- The thermal fraction that was estimated using two different methods (giving the complementary results) is about 0.17 (at 1.43 GHz), which is similar to that found in typical spiral galaxies. Also the total magnetic field strength (of about 7 μG), its ordered component (of about 3 μG), and degree of field order (of about 0.46), are typical for spiral galaxies, despite the low mass of NGC 2976.
- The analysis of rotation-measure distribution suggests the possible existence of a coherent, large-scale

[7] It should be noted that NGC 4605 has not been classified as the M 81 group member in the Karachentsev (2005) work. However, in a later paper Karachentsev & Kaisin (2007), it was included in the sample of group galaxies studied in Hα.

dynamo-generated magnetic field in NGC 2976. The dynamo number calculated for this low-mass galaxy greatly exceeds the critical value, indicating that, in this object, a large-scale $\alpha - \omega$ dynamo can indeed work efficiently. This is quite a surprising result, since sub-critical dynamo numbers were usually obtained for other dwarf galaxies studied to date.

- Re-imaging of the WSRT-SINGS data for NGC 2976 reveals a much more extended polarized signal than in the Heald et al. (2009) work, which is compatible with our sensitive VLA 1.43 GHz observations. The RM synthesis shows a single point component in the Faraday depth space. This confirms an RM distribution that was obtained by classical radio polarimetry from two frequencies (1.43 GHz and 4.85 GHz).
- The morphology of the magnetic field found in NGC 2976 does not resemble that expected for pure dynamo action since it features a polarized ridge in the south. This, along with an undisturbed optical appearance of the object, suggests that its magnetic field may 'remember' past tidal interactions with the M 81 galaxy (or the centre group galaxies). It is also possible that the ram pressure of the IGM could have further modified the morphology of the magnetic field observed in NGC 2976.
- The number of galaxies with a morphology similar to NGC 2976 in the M 81 group is not big enough to consider these objects an efficient source of magnetization of the intra-group medium. These galaxies (taking into account only the extension of their radio emission) can provide an ordered (or even regular) magnetic field to their neighbourhood up to distance of 5 kpc.
- A new weighting scheme, based on the quality of the individual frequency channels, for the RM synthesis algorithm was proposed and investigated. The application of this new weighting to the simulated data, as well as to the observed data, results in an improvement of the signal-to-noise ratio in the Faraday depth space.

Acknowledgements. We thank an anonymous referee for helpful comments and suggestions. This research has been supported by the scientific grant from the Polish National Science Centre (NCN), decision No. DEC-2012/07/N/ST9/04146. J.S.G.'s research on magnetic fields is partially supported through a Rupple Bascom Professorship that is generously funded by the University of Wisconsin-Madison. We acknowledge the use of the HyperLeda (http://leda.univ-lyon1.fr) and NED (http://nedwww.ipac.caltech.edu) databases.

References

Appleton, P. N., & van der Hulst, J. M. 1988, MNRAS, 234, 957
Appleton, P. N., Davies, R. D., & Stephenson, R. J. 1981, MNRAS, 195, 327
Beck, R., & Krause, M. 2005, Astron. Nachr., 326, 414
Beck, R., & Wielebinski, R. 2013, in Planets, Stars and Stellar Systems 5, eds. D. T. Oswalt, & G. Gilmore (Dordrecht: Springer), 641
Beck, R., Brandenburg, A., Moss, D., Shukurov, A., & Sokoloff, D. 1996, ARA&A, 34, 155
Brandenburg, A., & Subramanian, K. 2005, Phys. Rev., 417, 1
Braun, R., Heald, G., & Beck, R. 2010, A&A, 514, A19
Brentjens, M. A., & de Bruyn, A. G. 2005, A&A, 441, 1217
Briggs, D. S. 1995, Ph.D. Thesis, New Mexico Institute of Mining and Technology
Briggs, D. S., Schwab, F. R., & Sramek, R. A. 1999, in Synthesis Imaging in Radio Astronomy II, eds. G. B. Taylor, C. L. Carilli, & R. A. Perley, ASP Conf. Ser., 180, 127
Bronkalla, W., Notni, P., & Mutter, A. A.-R. 1992, Astron. Nachr., 313, 1
Bureau, M., & Carignan, C. 2002, AJ, 123, 1316
Calzetti, D., Kennicutt, R. C., Engelbracht, C. W., et al. 2007, ApJ, 666, 870
Chynoweth, K. M., Langston, G. I., Yun, M. S., et al. 2008, AJ, 135, 1983
Chyży, K. T. 2008, A&A, 482, 755
Chyý, K. T., & Buta, R. J. 2008, ApJ, 677, L17
Chyży, K. T., Beck, R., Kohle, S., Klein, U., & Urbanik, M. 2000, A&A, 355, 128
Chyży, K. T., Knapik, J., Bomans, D. J., et al. 2003, A&A, 405, 513
Chyży, K. T., Bomans, D. J., Krause, M., et al. 2007a, A&A, 462, 933
Chyży, K. T., Ehle, M., & Beck, R. 2007b, A&A, 474, 415
Chyży, K. T., Weżgowiec,M., Beck, R., & Bomans, D. 2011, A&A, 529, A94
Condon, J. J. 1987, ApJS, 65, 485
Dale, D. A., Cohen, S. A., Johnson, L. C., et al. 2009, ApJ, 703, 517
de Blok, W. J.G, Walter, F., Brinks, E., et al. 2008, AJ, 136, 2648
de Blok, W. J. G., Józsa, G. I. G., Patterson, M., et al. 2014, A&A, 566, A80
De Vaucouleurs, G., De Vaucouleurs, A., Corwin JR., et al. 1991, Third Reference Catalogue of Bright Galaxies, Version 3.9
Drzazga, R. T., Chyży, K. T., Jurusik, W., & Wiórkiewicz, K. 2011, A&A, 533, A22
Emerson, D. T., & Gräve, R. 1988, A&A, 190, 353
Gaensler, B. M., Haverkorn, M., Staveley-Smith, L., et al. 2005, Science, 307, 1610
Gallagher, J. S., & Matthews L. D. 2002, in Modes of star formation, ASP Conf. Proc., 285, 303
Gioia, I. M., Gregorini, L., & Klein, U. 1982, A&A, 116, 164
Gregory, P. C., & Condon, J. J. 1991, ApJS, 75, 1011
Gressel, O., Elstner, D., Ziegler, U., & Rudiger, G. 2008, A&A, 486, L35
Hanasz, M., Kowal, G., Otmianowska-Mazur, K., & Lesch, H. 2004, ApJ, 605, L33
Hanasz, M., Wóltański, D., & Kowalik, K. 2009, ApJ, 706, L155
Haslam, C. G. T. 1974, A&AS, 15, 333
Heesen, V., Rau, U., Rupen, M. P., Brinks, E., & Hunter, D. A. 2011, ApJ, 739, L23
Heald, G. 2008, in Cosmic Magnetic Fields: From Planets, to Stars and Galaxies, eds. K. G. Strassmeier, A. G. Kosovichev, & J. E. Beckman, Proc. IAU Symp., 259, 591
Heald, G., Braun, R., & Edmonds, R. 2009, A&A, 503, 409
Johnston-Hollitt, M., Hollitt, C. P., & Ekers, R. D. 2004, The Magnetized Interstellar Medium, eds. B. Uyaniker et al. (Katlenburg: Copernicus), 13
Jurusik, W., Drzazga, R. T., Jabłeka, M., et al. 2014, A&A, 567, A12
Karachentsev, I. D. 2005, AJ, 129, 178
Karachentsev, I. D., & Kaisin, S. S. 2007, AJ, 133, 1883
Kennicutt, R. C., & Evans, N. J. 2012, ARA&A, 50, 531
Kennicutt, Jr. R. C., Armus, L., Bendo, G., et al. 2003, PASP, 115, 928
Kennicutt, R. C., Lee, J. C.,Funes, S. J. et al. 2008, ApJ, 178, 247
Kepley, A. A., Mühle, S., Everett, J., et al. 2010, ApJ, 712, 536
Kronberg, P. P., Lesch, H., & Hopp, U. 1999, ApJ, 511, 56
Kulpa-Dybeł, K., Otmianowska-Mazur, K., Kulesza-Żydzik, B., et al. 2011, ApJ, 733, L18
Mao, S. A., Gaensler, B. M., Stanimirović, S., et al. 2008, ApJ, 688, 1029
Mao, S. A., McClure-Griffiths, N. M., Gaensler, B. M., et al. 2012, ApJ, 759, 25
Matthews, L. D., & van Driel, W. 2000, A&AS, 143, 421
Morsi, H. W., & Reich, W. 1986, A&A, 163, 313
Moss, D., Sokoloff, D., & Beck, R. 2012, A&A, 544, A7
Murphy, E. J., Kenney, J. D. P., Helou, G., Chung, A., & Howell, J. H. 2009, ApJ, 694, 1435
Niklas, S. 1995, Ph.D. Thesis, University of Bonn
Niklas, S., Klein, U., Braine, J., & Wielebinski, R. 1995, A&AS, 114, 21
Niklas, S., Klein, U., & Wielebinski, R. 1997, A&A, 322, 19
Otmianowska-Mazur, K., & Vollmer, B. 2003, A&A, 402, 879
Rudnick, L., & Owen, F. N. 2014, ApJ, 785, 45
Shukurov, A. 2007, in Mathematical Aspects of NaturalDynamos, eds. E. Dormy, & A. M. Soward (Boca Raton: CRC Press), 313
Siejkowski, H. 2012, Ph.D. Thesis, Jagiellonian University, Kraków
Simon, J. D., Bolatto, A. D., Leroy, A., & Blitz, L. 2003, ApJ, 596, 957
Soida, M., Beck, R., Urbanik, M., & Braine, J. 2002, A&A, 394, 47
Soida, M., Otmianowska-Mazur, K., Chyży, K. T., & Vollmer, B. 2006, A&A, 458, 727
Stil, J. M., & Israel, F. P. 2002a, A&A, 389, 29
Stil, J. M., & Israel, F. P. 2002b, A&A, 389, 42
Tabatabaei, F. S., Krause, M., Fletcher, A., & Beck, R. 2008, A&A, 490, 1005
Thilker, D. A., Bianchi, L., Meurer, G., et al. 2007, ApJS, 173, 538
Vollmer, B., Soida, M., Chung, A., et al. 2008, A&A, 483, 89
Vollmer, B., Soida, M., Chung, A., et al. 2010, A&A, 512, A15
Vollmer, B., Soida, M., Beck, R., et al. 2013, A&A, 553, A36
Walter, F. Brinks, E., de Blok, W. J. G., et al. 2008, AJ, 136, 2563
Widrow, L. M. 2002, Rev. Mod. Phys., 74, 775
Williams, B. F., Dalcanton, J. J., Stilp, A., et al. 2010, ApJ, 709, 135
Zeldovich, Ya. B., Ruzmaikin, A. A., & Sokoloff, D. D. 1990, The Almighty Chance (Singapore: World Sci.)

Appendix A: Application of radio interferometry weighting to RM synthesis

Processing spectro-polarimetric data using RM synthesis involves the application of frequency channel weighting. The method currently used (the so-called classic weighting scheme) consists of assigning weights of 1 to all the observed frequency channels and 0 to the others.

Obtaining the highest possible resolution in the Faraday domain requires observations in a wide spectral band. An example of this can be found in the WSRT-SINGS survey (Heald et al. 2009), where data were collected in the 18 and 22 cm bands, simultaneously. As only the weights of 1.0 or 0.0 are assigned to the particular frequency channels according to the classic weighting, it is highly desirable to obtain a uniform rms sensitivity across the observed band. However, in practice, it can be difficult to meet this criterion, which was the case also for the survey. Furthermore, sensitivities of individual channels within a single frequency band can considerably differ. This is often due to problems that are related to RFI or calibration errors. Thus, treating all (usable) frequency channels in the same way by assigning them the same weights of 1.0 does not seem to be the most adequate solution. In this appendix, we present a novel approach to weighting data in rotation measure synthesis, which permits the individual channel sensitivities to be taken into account.

A.1. Introduction to the new weighting scheme

Rotation measure synthesis is similar to radio interferometry (Brentjens & de Bruyn 2005). As such, one can try to write a formula for the RM Synthesis weight of j-th frequency channel in a similar way to the single visibility data point in imaging aperture synthesis observations (e.g. Briggs et al. 1999):

$$w_j(\lambda_j^2) = \frac{R_j(\lambda_j^2)T_j(\lambda_j^2)D_j(\lambda_j^2)}{\max(R_j(\lambda_j^2)T_j(\lambda_j^2)D_j(\lambda_j^2))}. \quad \text{(A.1)}$$

In radio interferometry these three elements (of imaging weight) are defined as follows: R_j describes reliability of a given visibility (it is related to the data quality), T_j is a tapering function (related to the position of a given data point in the uv-plane), and D_j is a density-weighting function. The last coefficient can be used to compensate a non-uniform distribution of data points in the UV-plane (for more details, see Briggs et al. 1999).

In RM synthesis, we can apply a similar weighting strategy and assume that R_j will describe a quality of an individual data point (i.e. Q and U Stokes parameters for a given frequency channel). We propose to approximate R_j by the following formula:

$$R_j(\lambda_j^2) = \frac{1}{\sigma_Q^2(\lambda_j^2) + \sigma_U^2(\lambda_j^2)}, \quad \text{(A.2)}$$

where, $\sigma_Q(\lambda_j^2)$ and $\sigma_U(\lambda_j^2)$ are the rms noise levels measured for a particular Q and U frequency channel, respectively. We chose $1/\sigma^2$ weighting, as it is widely used in statistical analysis and radio-interferometry (e.g. Briggs 1995; Briggs et al. 1999). Substituting $T_j = D_j = 1$ in formula (A.1) gives an equivalent of the so-called natural weighting of uv data points in aperture synthesis[8]. To test the new concept, we performed simple simulations of observations which are described below.

[8] We do not consider here cases where $T_j \neq 1$ and $D_j \neq 1$.

A.2. Simulations

In the simulations, we modelled the following three sources in the Faraday depth domain[9] (see Fig. A.2): a pointlike source located at a Faraday depth of -10 rad m^{-2} with flux of 10 Jy, a source extending from +30 to +50 rad m^{-2} with total flux of 40 Jy, and a source extending from +90 to +100 rad m^{-2} with a total flux of 30 Jy. These three sources (in the Faraday depth domain) are each seen as a single pointlike source in the sky plane.

For these sources, we simulated the spectro-polarimetric observations with a frequency setup similar to that used in the WSRT-SINGS survey (see Heald et al. 2009). Thus, we obtained two frequency bands (18 cm and 22 cm), each with 512 frequency channels. To simulate some diversity in the quality of the data channels (caused, e.g. by RFI), we increased noise levels in some of them. In particular, we increased noise from 2 to 10 times (randomly set) the standard value of 0.1 Jy/beam in 30% of the randomly chosen maps of the 18 cm band. Similarly, in the second band (22 cm), 10% of maps have 2 to 5 times higher rms values. For the data cubes that were simulated in this way (RA, Dec, frequency), the noise levels were measured in the off-source region and regarded as representative of the entire channel maps.

From these measurements, the channel weights were computed according to the formulas (A.1) and (A.2), assuming $T_j = D_j = 1$. For the data and weights prepared in this way, RM synthesis was performed using the software written by the authors.

We measured noise levels (in the same way as for RA, Dec, frequency data cubes) in the real and imaginary parts of the obtained Faraday dispersion function (RA, Dec, Faraday depth-data cubes, Fig. A.1). A comparison of these results with the analogous results calculated with classic (0 or 1) weighting shows that the rms values in the new approach are systematically lower. At the same time, the Faraday spectra obtained for the simulated sources (Fig. A.2) remain approximately the same for both the weightings (as expected). This implies that the net result of applying the new weighting is an increase of the signal-to-noise ratio. For these particular simulated data, the increase is about two times (the rms value is twice as low). We note that some small differences seen in the presented Faraday spectrum are due to the slightly different shapes of RMTFs that were obtained with both weightings (Fig. A.3). In fact, one would expect a wider main lobe of the RMTF when calculated with the new approach, as for the radio interferometry, where usually short baselines have more weight. This side effect is not visible for this particular setup as here data that possesses higher rms (lower weights) were generated with nearly uniform distribution in the simulated spectral band. A similar approach as that presented here to the data weighting was considered independently by Heald (2008) and Rudnick & Owen (2014), but few details are provided there.

A.3. Application of the new weighting scheme to the real data

To show how the proposed new weighting scheme in the RM synthesis works in practice, we re-analysed WSRT-SINGS data for galaxy NGC 2976. For comparison purposes, the dataset was processed in two ways. In the first approach, the classic weighting was applied with values 0 or 1. The second approach was based on the natural weighting (see above). Before applying

[9] Properties of the sources are exactly the same as in Appendix B of Brentjens & de Bruyn (2005).

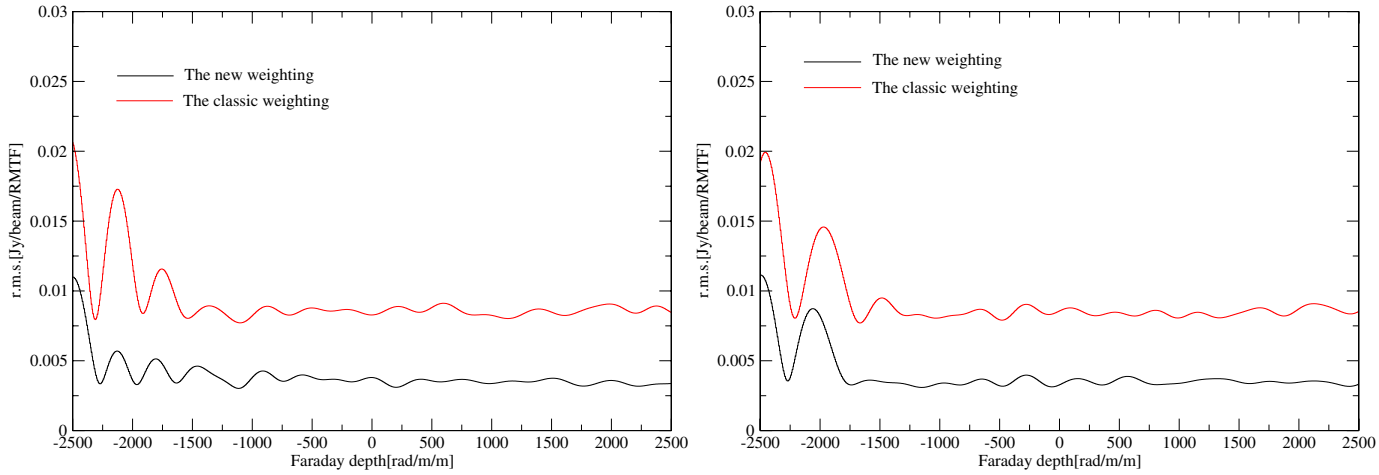

Fig. A.1. Rms noise levels for real (*left*) and imaginary (*right*) parts of the Faraday dispersion function. The measurements were performed in the same region as for the maps in the frequency domain.

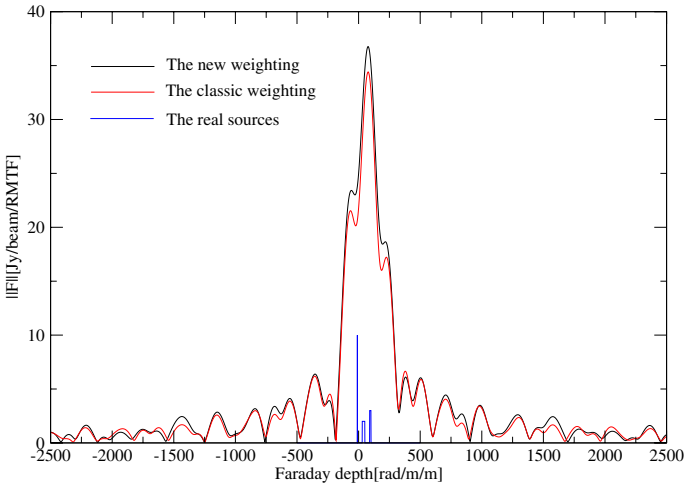

Fig. A.2. Faraday spectra obtained with the new (black) and the classic weighting (red) for the given sources (blue).

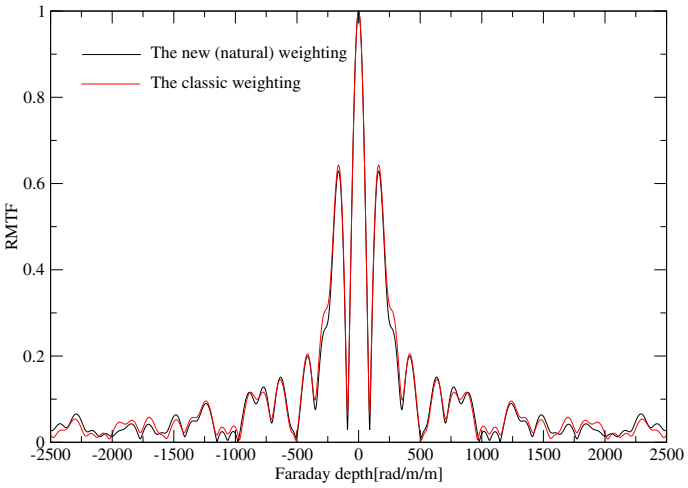

Fig. A.3. RMTF for the new (natural) and the classic weighting obtained for the simulated dataset (see text for details).

RM synthesis, the data for this galaxy were re-imaged and convolved to a resolution of about 45 (see Sect. 3.5 for a detailed description).

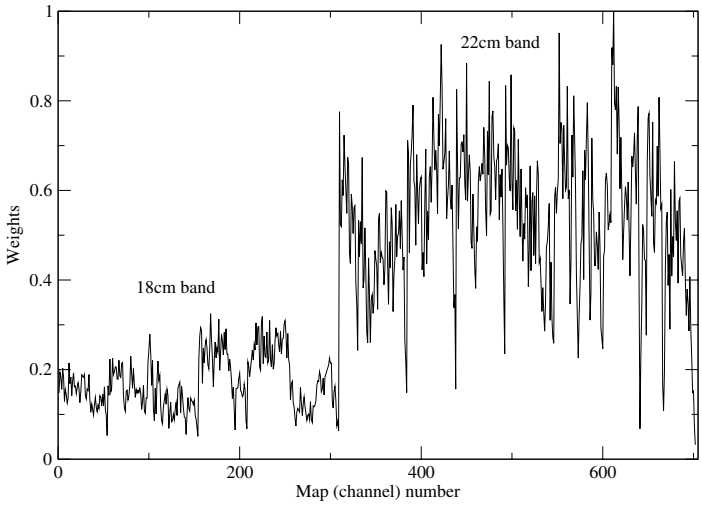

Fig. A.4. Weights computed according to formulas A.1 and A.2, assuming $T_j = D_j = 1$ versus map (channel) numbers.

The rms noise levels measured for particular Q and U Stokes parameters channel maps were computed in a polygon area, which was free of polarized emission and as close as possible to the phase centre. The latter criterion is important to minimize the influence of a primary beam's attenuation (which is frequency-dependent) on the obtained noise measurements. Having measured the noise levels, it was possible to calculate the weights according to the formulas (A.1) and (A.2) (Fig. A.4). We note that, in the 18 cm band, the weights are very low when compared to the 22 cm band. In the next step, the RM Synthesis was performed with the obtained weights included. The results of applying the new weighting scheme and the classic one are compared in Figs. 9 and A.5, where distributions of polarized emission and B-vectors are shown. As can be seen, there are less artifacts in the map obtained using the new weighting strategy. In fact, the noise level measured for this map is about 25 μJy/beam, while for the map obtained in the classic way, it is about 30 μJy/beam. Thus, because of taking into account the appropriate weights for each frequency channel, it was possible to reduce noise level in the resulting PI map by about 20%.

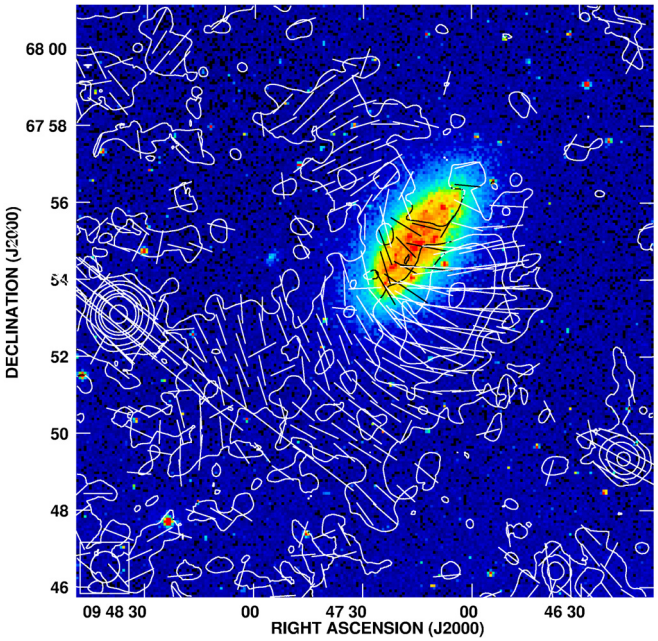

Fig. A.5. Polarized intensity contours and apparent B-vectors (not corrected for Faraday rotation) obtained with the classic weighting for NGC 2976 (WSRT-SINGS data) overlaid onto the DSS blue image. The contour levels and the beam size are the same as for Fig. 9.

A.4. Strong and weak points of the new weighting scheme

Increasing sensitivity of the Faraday dispersion function is the main advantage of the new weighting scheme. In this method, the best quality channels have the highest weights while the poorest ones are underweighted. It can be easily understood by recalling the fact that the rotation-measure synthesis is based on the Fourier transform, which in turn uses sine and cosine functions for a signal's sampling. The energy contained in these functions is infinite, because they are not limited to any particular λ^2. Thus the channels, which are less sensitive than the others, will limit sensitivity of the resulting power spectrum (the Faraday dispersion function). When we underweight these poor-quality channels, we also automatically limit the contribution of the high level of noise associated with them (and usually also some imaging artifacts) to the Faraday dispersion function. We note here that some factors, which could contribute to the reduction of noise level in our data, could be due to the particular dataset's channels that were assigned higher weights (22 cm) also having had a greater field of view.

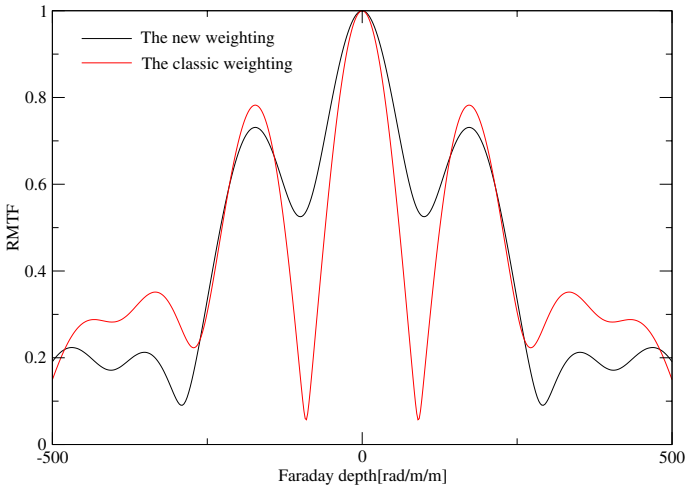

Fig. A.6. RMTF for RM Synthesis, performed for WSRT-SINGS data of NGC 2976 with the new and the classic weighting schemes.

Apart from sensitivity, the new weighting can also affect the shape of the rotation-measure transfer function. In Fig. A.6, both RMTFs, those obtained with the classic and the new weighting are presented. The latter shows a reduced level of side lobes (which is desirable) but, at the same time, their minima become much higher (which is not desirable). The other non-desirable effect is an increase of the width of the main lobe of RMTF in the new weighting (about 1.5 times), compared to the classic one.

It is also worth noting that the directions of B-vectors (not corrected for RM) on images (Figs. 9 and A.5) that were obtained with both methods differ by small amounts. This is due to the mean weighted λ^2 for which directions of B-vectors are computed not being the same in both approaches.